

Cite this: DOI: 00.0000/xxxxxxxxxx

A data-driven interpretation of the stability of organic molecular crystals

Rose K. Cersonsky,^{*a} Maria Pakhnova,^a Edgar A. Engel,^b and Michele Ceriotti^a

Received Date

Accepted Date

DOI: 00.0000/xxxxxxxxxx

Due to the subtle balance of intermolecular interactions that govern structure-property relations, predicting the stability of crystal structures formed from molecular building blocks is a highly non-trivial scientific problem. A particularly active and fruitful approach involves classifying the different combinations of interacting chemical moieties, as understanding the relative energetics of different interactions enables the design of molecular crystals and fine-tuning their stabilities. While this is usually performed based on the empirical observation of the most commonly encountered motifs in known crystal structures, we propose to apply a combination of supervised and unsupervised machine-learning techniques to automate the construction of an extensive library of molecular building blocks. We introduce a structural descriptor tailored to the prediction of the binding (lattice) energy and apply it to a curated dataset of organic crystals and exploit its atom-centered nature to obtain a data-driven assessment of the contribution of different chemical groups to the lattice energy of the crystal. We then interpret this library using a low-dimensional representation of the structure-energy landscape and discuss selected examples of the insights into crystal engineering that can be extracted from this analysis, providing a complete database to guide the design of molecular materials.

1 Introduction

Understanding molecular crystallization is critical to many fields of chemical sciences – from anticipating pharmaceutical stability and solubility^{1–5} to preventing⁶ or fostering⁷ aggregation in organic electronics to understanding complex formation in biological macromolecules^{8,9}.

Yet, molecular crystallization is a complex process that involves multiple cooperative and competing forces. Initial nucleation is typically motivated by strong interactions between functional groups^{10,11}. The structural patterns associated with these guiding interactions (deemed “supramolecular synthons”) and their hierarchies are often the focus of experimental and computational studies in crystal structure prediction^{12,13}. Nevertheless, once molecules have moved within closer range, many factors, including weaker interactions, the expulsion of solvent molecules, and geometric packing, will then determine the short- and potentially long-range order, leading to many potentially-stable polymorphs for a given stoichiometry. In the past decades, there has been a growing push to develop a “holistic” view of molecular crystallization^{14,15}, not only taking into account the nearest-neighbor contacts but also the interplay of these interactions with other components of the molecular assembly.

Thus, molecular crystallization has emerged as a hotbed for computational inquiry. While it is simpler to rationalize single-site interactions, the interplay of many competing interactions necessitates diverse, high-throughput studies¹⁴. This focus has led to considerable theoretical and software developments for qualitative and quantitative analyses, including those tailored to crystal structure prediction (CSP)^{16–19} and the representation of electrostatic surfaces and molecular geometry^{20,21}. Even more recently, machine learning has been used to understand the individual configurational and energy landscapes of molecules^{22–28}; however, such techniques have yet to be applied in the general, holistic vein required to extract the qualitative insights that can be used to support crystal design efforts.

To study molecular crystallization in this broad lens, we have curated a dataset of roughly 3'260 C+H+N+O+S-containing molecular crystals from those reported in Cordova *et al.*²⁹. In Cordova *et al.*²⁹, these crystals were initially selected by querying the Cambridge Structural Database (CSD) to identify a diverse set of synthesizable molecular assemblies, including those originally experimentally stabilized at extreme conditions. The experimental properties of the full dataset are summarized in Appendix A3.

The stability of molecular crystals is traditionally studied through the binding (lattice) energy, which is computationally determined by computing the ground-state energies for both the crystal and its molecular components in the dilute gas limit, here computed using DFT-PBE-D2 calculations of each crystal and its relaxed molecular components at ambient conditions.

^a Laboratory of Computational Science and Modeling (COSMO), École Polytechnique Fédérale de Lausanne, Lausanne, Switzerland

^b TCM Group, Trinity College, Cambridge University, Cambridge, UK

* Present address: Rose.Cersonsky@wisc.edu

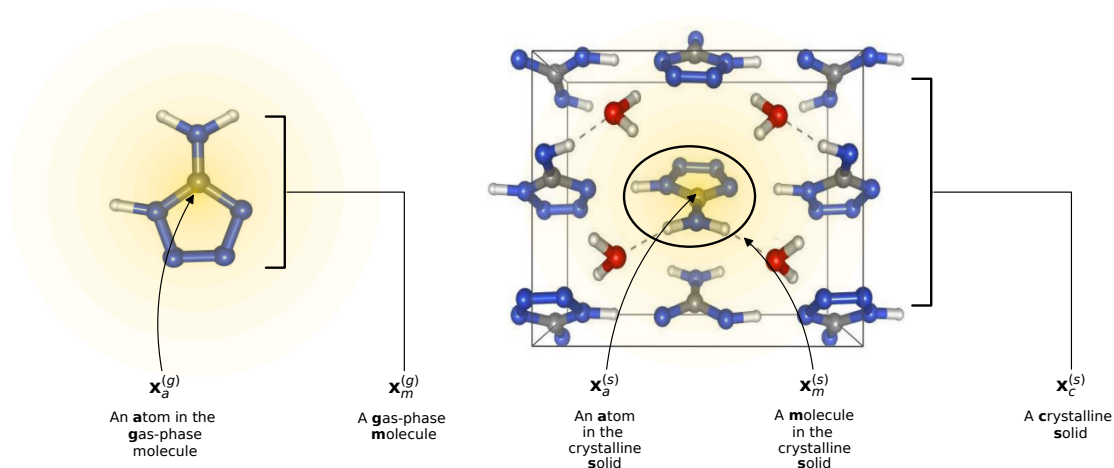


Fig. 1 Visualization of Descriptor Notation, as described in Sec. 2.1, visualized for 5-Aminotetrazole Monohydrate (CSD Ref. AMTETZ³⁰). Each descriptor contains the information of an atom and its neighborhood (shown in yellow shading).

From here, we build an atom-centered regression model for this lattice energy, demonstrating the improvements in accuracy and reduction in model complexity from using a physics-informed approach. This atom-centered approach, wherein we represent each molecular crystal using the average ML descriptor for each of its atomic constituents, facilitates estimating the contribution of each atom, or combination of atoms, to the binding energy. Then, employing a combination of supervised and unsupervised machine learning models, we can determine and interpret each molecular moiety’s intermolecular interactions. Using these approaches, we show how physically-motivated machine learning models can not only “rediscover” the known maxims of crystal engineering, but provide insight and guidance for crystal design. We have made our datasets, and analyses openly-available through the Materials Cloud³¹, with interactive components aimed to guide future molecular design and narrower or targeted studies.

2 Notation

In this study, we employ atom-centered descriptors³² to identify the contributions of specific collections of atoms to the binding of a crystal. Given the many atomic and energetic entities (atoms, molecules, crystals, total energy versus lattice energy), we rely on many numerical representations and equations; hence we start by establishing a consistent notation we will use throughout the text.

2.1 Descriptors

To reflect the physics of atomic interactions, we use symmetry-adapted descriptors to encode/describe the geometric arrangement of atoms in their atomistic configurations, specifically the 3-body SOAP descriptors outlined in Appendix B1. Each of these input descriptors is written as $\mathbf{x}_\sigma^{(i)}$, where the subscript σ signifies the collection of atoms being described, including the entire crystal (c), a molecule (m), or an atom (a). n_σ is the number of atoms in the given collection. Thus it follows that n_c is the number of atoms in a given crystal, and n_m is the number of atoms in a given molecule. Because we discuss analogous atoms or molecules in both the solid and gas phases, we use the super-

script (i) to denote the phase (crystalline solid (s) or dilute gas (g)).

The descriptor for a given collection should be assumed as the average of the descriptors for the constituent atoms:

$$\mathbf{x}_\sigma^{(i)} = \frac{1}{n_\sigma} \sum_{a \in \sigma} \mathbf{x}_a^{(i)}. \quad (1)$$

For example, the descriptor for the atoms in a molecule in a dilute gas is $\mathbf{x}_m^{(g)} = \frac{1}{n_m} \sum_{a \in m} \mathbf{x}_a^{(g)}$. If we were to look at the same molecule in the crystalline solid we would get $\mathbf{x}_m^{(s)} = \frac{1}{n_m} \sum_{a \in m} \mathbf{x}_a^{(s)}$. A schematic of these concepts is shown in Fig. 1, using the co-crystal 5-Aminotetrazole Monohydrate (CSD Ref. AMTETZ³⁰) as an example.

2.2 Energies and Regressions

We use \mathbf{E}_σ to denote the total energy of a collection of atoms. In this study, the total energies of the crystals \mathbf{E}_c are taken from those reported in Cordova *et al.*²⁹ and the total energies of the molecules \mathbf{E}_m are determined by DFT-PBE-D2 calculations, as described in Appendix A2. We use $e_\sigma \equiv \mathbf{E}_\sigma / n_\sigma$ to indicate the per-atom energy. Note that we express all energies in kJ/mol, where e_σ is to be interpreted as having the units of kJ/mole of atoms. Constructing a linear regression amounts to the ansatz

$$\mathbf{e}_\sigma = \mathbf{x}_\sigma \mathbf{w}_\sigma + \epsilon_\sigma \quad (2)$$

where \mathbf{w}_σ is the regression weights and ϵ_σ the residual errors. The *lattice energy* (also referred to as the *binding* or *cohesive energy* in literature) of a molecular crystal is given by Δ_c , where

$$\Delta_c = \mathbf{E}_c - \sum_{m \in c} \mathbf{E}_m. \quad (3)$$

With the average lattice energy per atom given by

$$\delta_c \equiv \Delta_c / n_c = \mathbf{e}_c - \sum_{m \in c} \frac{n_m}{n_c} \mathbf{e}_m \quad (4)$$

Regression Equation	Eq.	RMSE	MAE
$\mathbf{e}_c = \mathbf{x}_c^{(s)} \mathbf{w}_c$	(2)	1.15	0.863
$\mathbf{e}_m = \mathbf{x}_m^{(g)} \mathbf{w}_m$	(2)	0.727	0.563
$\delta_c = \mathbf{x}_c^{(s)} \mathbf{w}_c - \sum_{m \in c} \frac{n_m}{n_c} \left(\mathbf{x}_m^{(g)} \mathbf{w}_m \right)$	(6)	0.916	0.652
$\delta_c = \mathbf{x}_c^{(s)} \mathbf{w}$		0.778	0.552
$\delta_c = \mathbf{x}_c^{(g)} \mathbf{w}$		1.101	0.723
$\delta_c = \mathbf{x}_c^{(s-g)} \mathbf{w}$	(9)	0.571	0.404
$\delta_c = \{ \mathbf{x}_c^{(s)}, \mathbf{x}_c^{(g)} \} \mathbf{w}$		0.671	0.461

Table 1 Results of Linear Regression Exercises. In each linear regression, an independent, 5-fold cross-validated model was built on 2'707 crystals (or the 3'242 coinciding molecules). Here we report the errors (in kJ/mol) on a separate set of 551 crystals (or the coinciding 628 molecules). In each regression equation \mathbf{w} is unique to that regression.

Later, we will use our regression model to determine the atomic contributions to the lattice energy, which we will denote δ_a , where $\delta_c = \frac{1}{n_c} \sum_{a \in c} \delta_a$. We will also consider the contributions for different collection of atoms, and will denote the average lattice energy contribution as $\delta_\sigma = \frac{1}{n_\sigma} \sum_{a \in \sigma} \delta_a$. When we regularize these contributions using a Gaussian filter (discussed in Sec. 3.2 and Appendix B2), we will use a tilde to give $\tilde{\delta}$.

3 Results and Discussion

In the following, we consider crystals and gas-phase molecules, both of which have been geometry-optimized by minimizing their configurational energies with respect to the atomic positions, as described in Appendix A. Unless stated otherwise, we use as our featurization the 3-body SOAP vectors (as described in Appendix B1) and build a regularized ridge regression models using `scikit-learn`³³. All models were trained on the same training set of 2'707 crystals (or the corresponding 3'242 molecules). We report errors on a mutually-exclusive set of 551 crystals (or the corresponding 628 molecules). When interpreting the results, it is important to consider that the test set has been selected at random, and is therefore representative of the makeup of the GSD, while the training structures were selected with Farthest Point Sampling^{34,35} to maximize the diversity, and therefore contain a large fraction of unstable, "extreme" cases.

3.1 Building a Model for the Lattice Energy

One can estimate the atomic contributions to a target property (and thereby assess the contributions of specific molecular motifs) by building a robust machine learning model on an atom-centered descriptor³⁶. Suppose we have a descriptor

$$\mathbf{x}_\sigma = \frac{1}{n_\sigma} \sum_{a \in \sigma} \mathbf{x}_a \quad (5)$$

and train a regression model on some target \mathbf{y} such that $\mathbf{y} = \mathbf{x}_\sigma \mathbf{w} + \epsilon$, where \mathbf{w} is the regression weight and ϵ is the residual error from the regression. We can then estimate the approximate

contribution of each atom by computing $\mathbf{y}_a = \mathbf{x}_a \mathbf{w}$.

Combining models of \mathbf{e}_c and \mathbf{e}_m Given Eq. (4), it is possible to build a model for the lattice energy from two separate models for crystal and molecular energy, replacing each energy \mathbf{e} with its approximation via linear regression (Eq. (2))

$$\delta_c = \mathbf{x}_c^{(s)} \mathbf{w}_c + \epsilon_c - \sum_{m \in c} \frac{n_m}{n_c} \left(\mathbf{x}_m^{(g)} \mathbf{w}_m + \epsilon_m \right). \quad (6)$$

Eq. (6) may then be rewritten as:

$$\delta_c = \mathbf{x}_c^{(s)} \mathbf{w}_c - \mathbf{x}_c^{(g)} \mathbf{w}_m + \epsilon \quad (7)$$

where we have defined $\epsilon \equiv \epsilon_c - \sum_{m \in c} \frac{n_m}{n_c} \epsilon_m$. In this scheme, the regression of the lattice energy is implicitly limited by the errors of the independent regressions; therefore, if we obtained a good fit for \mathbf{e}_c and \mathbf{e}_m , this should be a fairly robust way to predict the lattice energy.

When we predict the crystal and molecular atomic energies \mathbf{e}_c and \mathbf{e}_m , we obtain RMSEs of 1.15 kJ/mol and 0.727 kJ/mol, respectively, which are acceptably small compared to the intrinsic variance of the baselined* target energies of the test set, which have standard deviations of 4.402 kJ/mol and 4.251 kJ/mol, respectively. However, the intrinsic variance of the lattice energies is smaller (1.965 kJ/mol); therefore, the resulting RMSE of 0.916 kJ/mol from Eq. (6) is very unsatisfactory and suggests that the errors in the independent regressions generally overlap with the lattice energy contributions.

Building a model directly on δ_c With the reduced variance of the target (lattice energy), it thus makes sense to construct the regression model directly on our target. Building a regression on the gas-phase descriptors $\mathbf{x}_c^{(g)}$, while conceptually nonsensical (the descriptors of the molecules contain no information on the intermolecular interactions), yields an RMSE of 1.101 kJ/mol. Regressing on the solid-phase descriptors $\mathbf{x}_c^{(s)}$ improves the regression substantially, achieving an RMSE of 0.778 kJ/mol.

Yet, conceptually, neither of these two representations ($\mathbf{x}_c^{(s)}$ and $\mathbf{x}_c^{(g)}$) contain the full set of relevant information – the molecular descriptor $\mathbf{x}_c^{(g)}$ is missing information on intermolecular interactions, and the crystal descriptor $\mathbf{x}_c^{(s)}$ is unaware of the conformational changes that the molecules undergo upon crystallization. The necessity of this missing information is confirmed when we regress on concatenated descriptors $\{ \mathbf{x}_c^{(s)}, \mathbf{x}_c^{(g)} \}$ and our RMSE drops to 0.671 kJ/mol.

Furthermore, Eq. (7) provides another way to similarly (and more explicitly) encode the nature of the problem into our choice of representation. Given a descriptor that appropriately distinguishes between periodic crystals and molecules, a regression model can predict their energies using the same regression

* To improve the regressions of crystal and molecular energies, we subtract a *baseline* determined by linear regression of the atomic composition on the total energies.

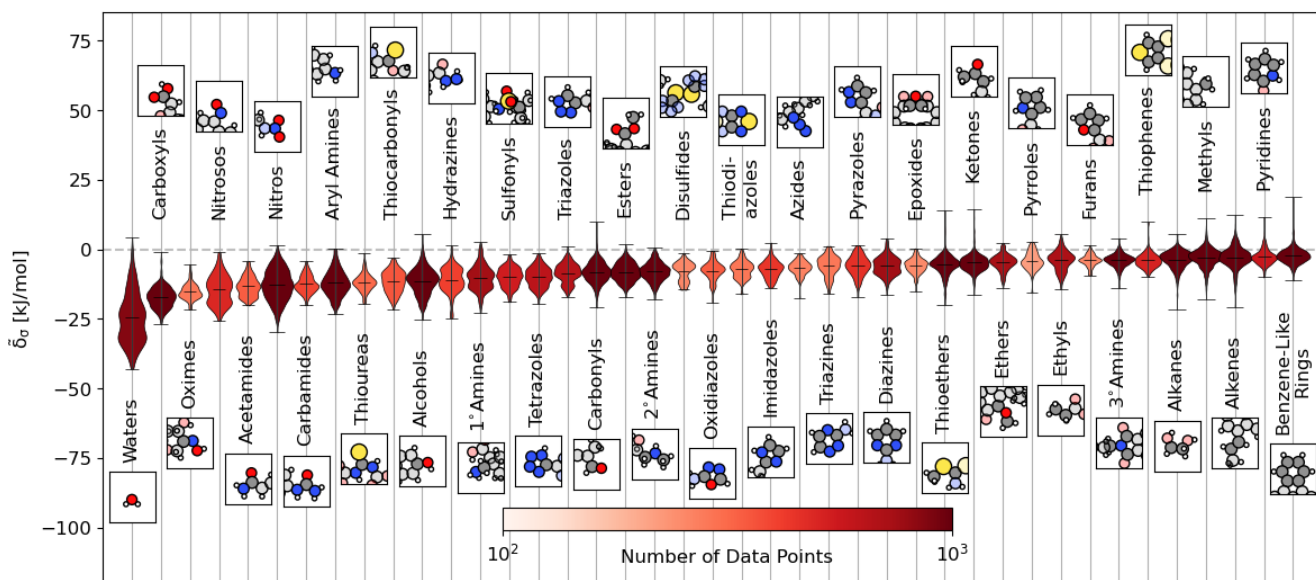


Fig. 2 Distribution of Energetic Contributions for Different Functional Groups. For each functional group, we have taken the averaged remnant descriptor $\mathbf{x}_\sigma^{(s-g)}$ and computed the estimated contribution to the binding energy $\bar{\delta}_\sigma$ using the regressions detailed in Eq. (10) and the filtering procedure in Eq. (11)

. We have arranged the functional groups in order of average contribution, with a representative example is shown above or below the violin plot with the functional group highlighted. We have limited this figure to those functional groups with more than 200 instances in the dataset (see Figure S4 for all groups). The lines on each plot denote each group’s extreme and mean contributions. The plots are colored by the number of examples within the dataset, ranging from 4 (pentazole) to 5313 (methyl groups). Wider sections of the violin plot represent a higher probability that members of the population will take on the given value; the skinnier sections represent a lower probability.

weights, $\mathbf{w} = \mathbf{w}_c = \mathbf{w}_m$. Substituting this into Eq. (7),

$$\delta_c = \mathbf{x}_c^{(s)} \mathbf{w} - \mathbf{x}_c^{(g)} \mathbf{w} + \epsilon \quad (8)$$

$$= \mathbf{x}_c^{(s-g)} \mathbf{w} + \epsilon \quad (9)$$

where we define $\mathbf{x}_c^{(s-g)} \equiv (\mathbf{x}_c^{(s)} - \mathbf{x}_c^{(g)})$ as the so-called “remnant” descriptor and ϵ again denotes the residual errors. Explicitly adapting our representation $\mathbf{x}_c^{(s-g)}$ to the nature of the lattice energy results in a yet better result to learning on $\{\mathbf{x}_c^{(s)}, \mathbf{x}_c^{(g)}\}$: 0.571 kJ/mol, despite being in a smaller feature space. Conceptually, this descriptor still encodes the 3-body correlation between an environment and its neighbors but explicitly incorporates the change in molecular geometry upon crystallization and reduces the weights of atomic triplets whose interactions are primarily intramolecular and/or the same in gas and solid phase.

Extension to non-linear models This result is mirrored in non-linear regression models, where again, a superior result is obtained by either constructing a kernel on $\mathbf{x}_c^{(s-g)}$ or taking the difference of non-linear feature vectors (see Appendix C2). An optimized RBF kernel on the remnant descriptors yields a similar RMSE to the linear model, likely due to the restricted dataset size and diversity. We get some improvement (by ~ 0.06 kJ/mol compared to the best linear model) by taking the difference of the non-linear features defined by the kernels of the crystalline and molecular descriptors. This result further emphasizes the rationale behind the remnant approach, and suggests that one can

improve accuracy by combining non-linear feature constructions to mimic the mathematical formulation of target properties. To show that kernel optimization has little impact on this conclusion, we have also included corroborating results using a parameter-free kernel, also in Appendix C2.

When the molecular geometry is known *a priori*, these results suggest that linear and non-linear regressions for the lattice energy should be built on descriptors conceptually akin to $\mathbf{x}_c^{(s-g)}$, rather than $\mathbf{x}_c^{(s)}$, as has been common practice in the literature^{23,25,27,28}. Thus, in the remainder of the text, we will employ ML fingerprints and models based on the remnant descriptor.

3.2 Estimating the contributions of molecular motifs

Regularizing the Atomic Contributions With our target-adapted regression model, we can assign effective contributions to each atomic environment, where we take the remnant descriptor of each atomic environment and compute

$$\delta_a = \mathbf{x}_a^{(s-g)} \mathbf{w}. \quad (10)$$

Despite the mathematical logic behind this step, the lack of physical underpinnings for this decomposition may result in energy being arbitrarily partitioned between neighboring atoms. This leads to disproportionately large contributions of opposite size being assigned, not dissimilar to how a regression may overfit by assigning large regression weights. To ease this effect, we can apply

a Gaussian filter to each δ_a . For the i^{th} atom, this results in

$$\tilde{\delta}_i = \sum_j \delta_j \frac{f(i,j)}{\sum_k f(j,k)} \quad (11)$$

where \sum_j runs over all neighbors of i and \sum_k runs over all neighbors of j (defined by a cutoff of 2\AA). For neighbors a and b and interatomic distance d_{ab} , $f(a,b) = \exp[-d_{ab}^2/2\sigma^2]$. This procedure, introduced for the electronic density of states in Ben Mahmoud *et al.*³⁷, has the effect of regularizing the decomposition while maintaining the regression results, *i.e.*, $\delta_c = \frac{1}{n_c} \sum_{a \in c} \delta_a = \frac{1}{n_c} \sum_{a \in c} \tilde{\delta}_a$. We show this effect of the filter on the distribution of atomic contributions in Appendix B2. It is worth to compare our data-driven decomposition with one based on an empirical model of interactions, or with one of the many atoms-in-molecules decompositions of the energy computed by quantum-chemical calculations. On one hand, our approach makes it harder to explicitly interpret the stabilizing power of a motif in terms of physical terms (electrostatics, dispersion...). On the other, in many cases forcefields and energy decompositions have a high degree of arbitrariness, and the accurate prediction of the total binding energy comes from a cancellation of errors in the individual components. The atomic contributions Eq. (11) are obtained with the only requirement of being smooth, and (since they are built using a remnant descriptor) to correlate with the structural features associated with the crystal-forming process. As we shall see, their nature allows one to recognize the role played by collective effects - such as steric hindrance, or molecular distortions - contributing to our goal of a holistic view of lattice stability.

Visualizing the Contributions of Different Motifs Taking the 3'242 molecules from our training set, we use SMARTS descriptors³⁸ and RDKit Substructure Matching³⁹ to identify the atoms belonging to common molecular motifs, finding 46'010 motifs. Details of this procedure and our table of SMARTS strings are given in Appendix B3 and Table S3, respectively. For each motif, we determine the effective cohesive interaction $\tilde{\delta}_\sigma$ as[†]

$$\tilde{\delta}_\sigma = \frac{1}{n_\sigma} \sum_{a \in \sigma} \tilde{\delta}_a \quad (12)$$

We plot the span of lattice energy contributions for motifs with greater than 200 instances in the dataset in Fig. 2. The functional groups are arranged in order of increasing average cohesive interactions. Nearly all functional groups, on average, are stabilizing, although we see a clear trend in the nature of the functional groups from left to right. On the left (the motifs leading to the strongest intermolecular interactions), there are groups typically associated with hydrogen bonding (*e.g.*, carboxyls and waters). As we move to the right, the molecular motifs are, on average, weakly binding, with the largest range of interactions coming from the most broadly-defined groups, including the alkanes, alkenes, and benzene-like rings.

This trend is further demonstrated by plotting the structure-

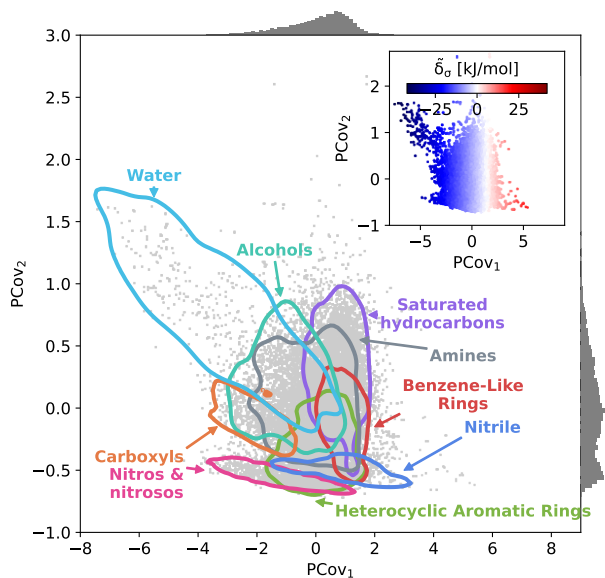


Fig. 3 Principal Covariates Regression (PCovR) Map of the Interactions of Molecular Motifs. A structure-property map of molecular motifs, denoting major classes of motifs and outlining the regions where the 90th percentile of these motifs occur. (inset) the same map colored by the cohesive interactions, ranging from blue (strongly attractive) to white (neutral) to red (strongly resistant). Histograms on the upper and right borders show the distribution of motifs along the covariates.

property map of all motifs using *Principal Covariates Regression* (PCovR), a hybrid supervised-unsupervised dimensionality reduction technique first introduced in De Jong and Kiers⁴⁰ and adapted to chemical systems in Helfrecht *et al.*⁴¹ This technique produces a latent-space mapping that arranges different motif classes based on their structural similarity and correlation to a set of target properties. In Fig. 3, we show a map using the average remnant descriptor for each motif and their average energy contribution, using contour lines to show where 90% of such motifs fall on the PCovR map. One sees that, in this case, the first axis of this plot (PCov₁) correlates strongly with the (learnable) cohesive interactions. The second axis (PCov₂) allows us to resolve structural differences between motifs with similar energetic contributions. In this mapping, we can learn from the spread of each group. For example, the 868 water molecules (light blue in Fig. 3) span the greater portion of the left-hand side of the figure, highlighting the chemical diversity of intermolecular water interactions. Juxtapose this with the 2'627 nitro and nitroso groups (pink in Fig. 3) that span a smaller region in PCovR space, implying a narrower range of intermolecular interactions. Here we have combined several groups for visual simplicity; however, we have included plots highlighting each functional group in Figs. S6-S9, including the sample sizes and range of contributions.

The PCovR framework also provides a blueprint for analyzing the interactions of different structural motifs – given a single motif type, what characteristics of a molecular environment lead to a more stabilizing interaction? In the following sections,

[†] The lattice energy of the crystal is not the sum of these motif contributions, as 1) both are averaged quantities, and 2) a single crystal may have overlapping motifs.

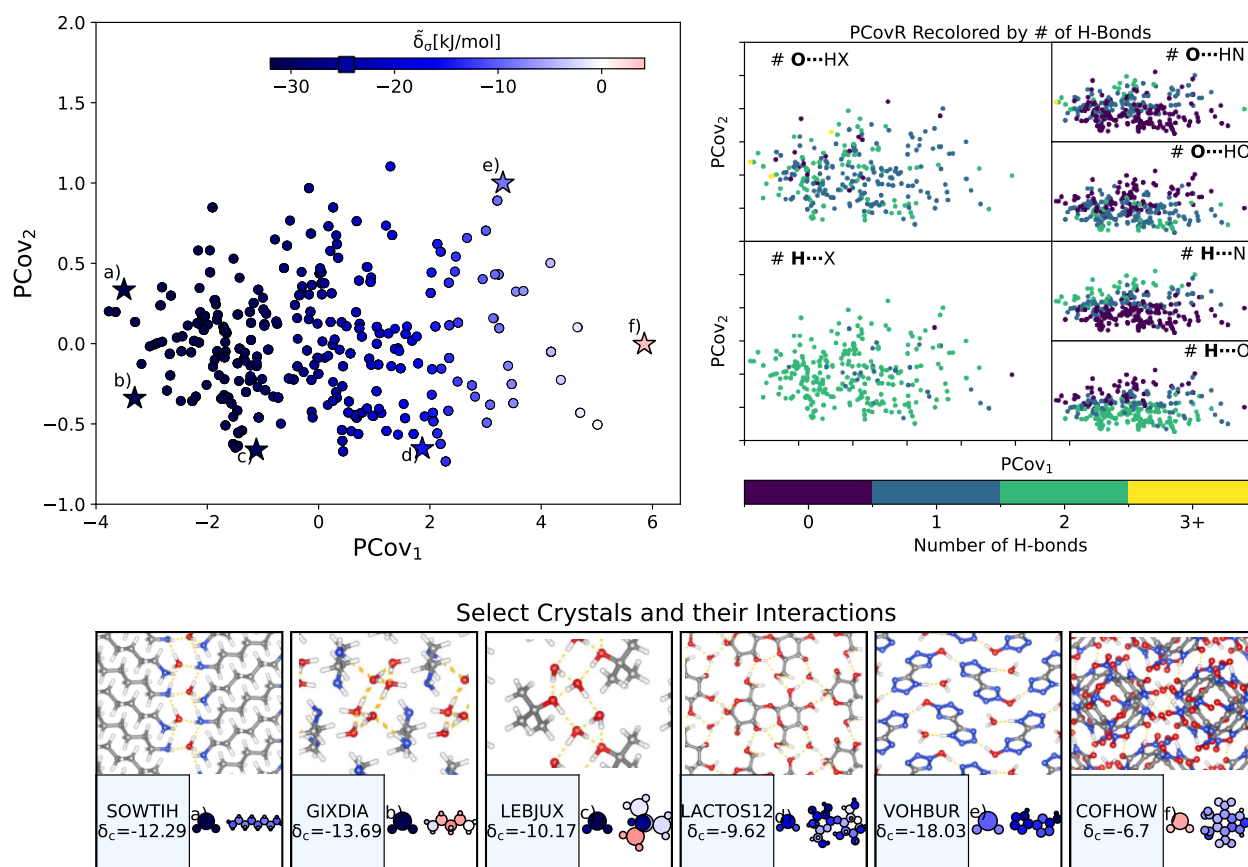


Fig. 4 The Interactions of Water Molecules. (left) Principal Covariates Regression (PCovR) map, where the color of each point denotes the estimated cohesive interaction of that motif and a marker on the color bar denotes the average value for all waters. (right) The PCovR map recolored by the number of hydrogen bonds (H-bonds), separating those donated to the oxygen atom (top) from those donated by the hydrogen atoms (bottom). The insets on the bottom visualize several extremal or interesting environments. Select crystalline configurations and energy assignments: CSD Refs. (a)SOWTIH⁴², (b)GIXDIA⁴³, (c)LEBJUX⁴⁴, (d) LACTOS12⁴⁵, (e) VOHBUR⁴⁶, and (f) COFHOW⁴⁷. In each panel, the bottom row shows the total lattice energy of the crystal (in kJ/mol) and the corresponding molecules where the atoms have been recolored by their estimated lattice energy contribution (on the same scale as on the PCovR map).

we will take a look at the stabilizing environments for a few classes of functional groups, starting with the well-known stabilizing interactions of water and carboxylic groups, then moving onto two groups with a wide range of intermolecular interactions, 6-membered aromatic carbon rings and nitro groups. With each functional group, we generate a new PCovR only using the averaged remnant descriptors and effective interactions for the instances of that group, such that the structural diversity embedded in the map reflects the diversity of *interactions*, rather than the diversity of the molecules. We have included similar maps for all other molecular motifs in an online data repository^{31,48}.

3.2.1 Waters

We begin with a ubiquitous molecular crystal stabilizer: water. The estimated contributions of the 868 water molecules in this dataset span a range of -42.92 to 4.16 kJ/mol (e of atoms), with the majority of interaction strengths occurring at around -24.65 ± 9.06 kJ/mol. We generate a new PCovR shown in the left panel of Fig. 4. On the bottom of Fig. 4, we show the crystalline conformation and the molecules recolored by δ_a .

First, we look at a common parameter for measuring the sta-

bilizing effect of water: hydrogen bonding (H-bonding). Here, we have calculated H-bonds based on when the $O \cdots H$ or $H \cdots X$ distance is less than 2.5 \AA and the dihedral angle of $O \cdots H-X$ or $OH \cdots X$ is greater than 150° . From the right side of Fig. 4, we see that the number of H-bonds donated to the water molecule ($O \cdots H$) does not correlate with the cohesive interaction of the water molecules. There is some qualitative correlation/anti-correlation between the nature of these donated H-bonds and the second principal covariate (Pearson Correlation Coefficient, or PCC, $=0.49, -0.59$ for the number of $O \cdots H-N$ and $O \cdots H-O$, respectively). There is a mild anti-correlation between the number of H-bonds the water itself donates ($OH \cdots X$) and the first covariate, with a PCC of -0.33 . The second principal covariate is strongly correlated and anti-correlated with the number of $OH \cdots N$ and $OH \cdots O$ interactions, achieving a PCC of 0.69 and -0.73 , respectively. Waters with primarily $OH \cdots N$ -type hydrogen bonds are at the top of the map (e.g., Fig. 4(e), CSD Ref. VOHBUR⁴⁶), with $OH \cdots O$ -type at the bottom of the map (e.g., Fig. 4(c-d), CSD Refs. LEBJUX⁴⁴ and LACTOS12⁴⁵).

This analysis emphasizes that the number of hydrogen bonds does not fully capture all of the nuances of water stabilization –

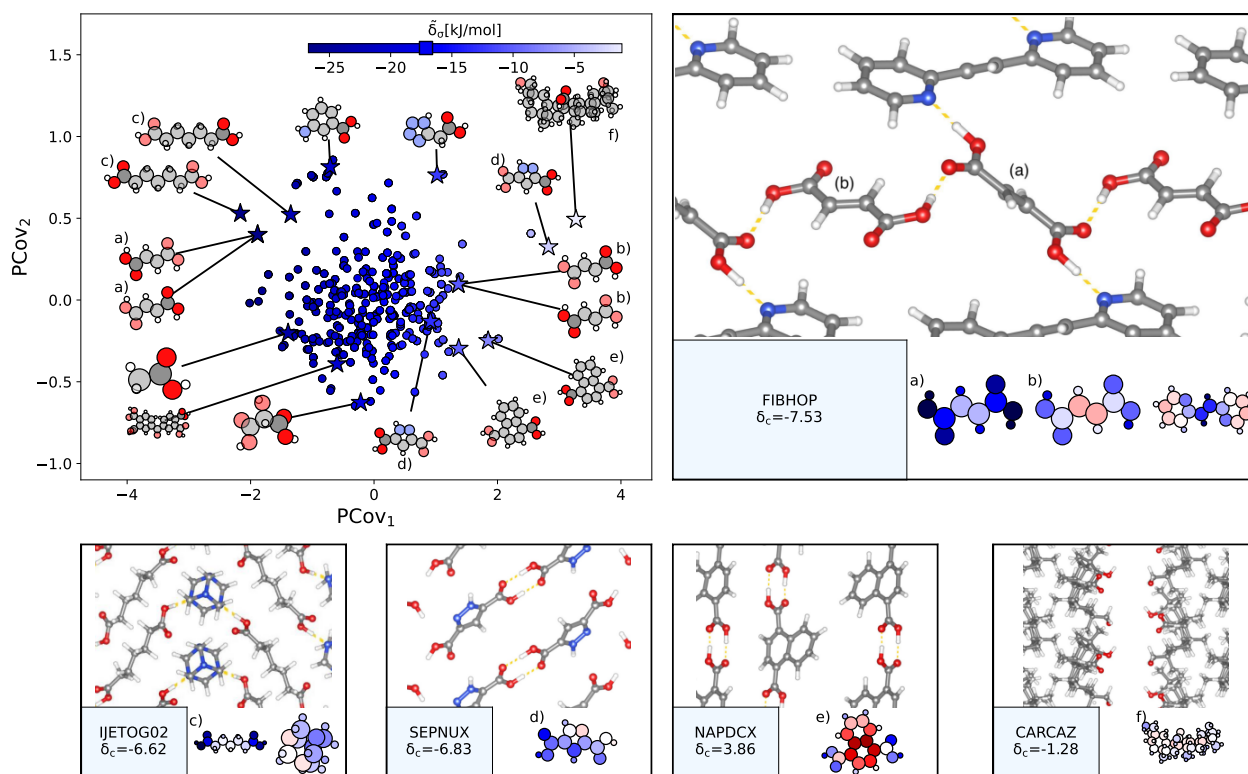


Fig. 5 The Interactions of Carboxylic Acid Groups. (left) Principal Covariates Regression (PCovR) Map, where the color of each point denotes the estimated cohesive interaction of that motif, and a marker on the color bar denotes the average value for all carboxylic acid groups. The insets visualize several extremal or interesting motifs. (right) Select crystalline configurations and energy assignments: CSD Refs. (a,b) FIBHOP⁴⁹, (c) IJETOG02⁵⁰, (d) SEPNUX⁵¹, (e) NAPDCX⁵², and (f) CARCAZ⁵³. In each panel on the right, the bottom row shows the total lattice energy of the crystal (in kJ/mol) and the corresponding molecules where the atoms have been recolored by their estimated lattice energy contribution.

the majority of water molecules participate in 2-3 such interactions, and the energy of these bonds can span a wide range. In $O \cdots H-X$ interactions, there is little energetic difference based on whether the acceptor is a nitrogen or oxygen atom – both types of hydrogen bonds span the full range of energies. The nature of the acceptor is encoded in the covariate orthogonal to the chemical features most correlated with interaction strength (*i.e.*, the nature of the acceptor is primarily correlated with the second covariate).

We see that the strongest water interactions in 1,6-Diaminohexane monohydrate (CSD Ref. SOWTIH⁴², Fig. 4(a)) and 1,3-Diaminopropane trihydrate (CSD Ref. GIXDIA⁴³, Fig. 4(b)), where the water molecules associate with other water molecules and the amine group of their co-crystalline molecule. Our weakest contribution, by far, occurs in 4,5,6,7-Tetranitro-1,3-dihydro-2H-benzimidazol-2-one hemihydrate (CSD Ref. COFHOW⁴⁷, Fig. 4(f)), where the water molecules sit interstitial to the imidazole molecules, prohibited from forming hydrogen bonds and potentially interfering with the stabilization of the imidazole clusters.

3.2.2 Carboxylic Acid Groups

As a strong electron donor, carboxylic acids are considered a key motif in molecular crystallization^{21,54,55}, which is supported by their strong negative lattice energy contribution, here ranging from -26.72 kJ/mol to -1.11 kJ/mol, with the majority of inter-

action strengths occurring in the -17.17 ± 3.82 kJ/mol range. Taking the 1'023 carboxylic acid groups, we generate a new PCovR shown in the left panel of Fig. 5. On the right and bottom of Fig. 5, we have included panels showing, for select motifs, the crystalline conformation and molecules recolored by δ_a .

The strongest contributions are found in 1,2-Di(2-pyridyl)ethylene (CSD Ref. FIBHOP⁴⁹) in a succinic acid molecule (Fig. 5(a)) that forms two sets of supramolecular synthons: one homosynthon with the other succinic acid (Fig. 5(b)), and one heterosynthon with the pyridine group (consistent with the literature on the strength of carboxylic-pyridine interactions⁵⁶⁻⁵⁸). Interestingly, this crystal also contains one of the most weakly interacting groups (Fig. 5(b)), in the second succinic acid molecule that only participates in the single homosynthon.

Carboxylic acids form the strongest cohesive interactions when participating in multiple synthons, particularly heterosynthons (and typified by Fig. 5(a) and (c), and noted in earlier literature⁶⁴). Moving to the right, we see the contribution decrease commensurate to the number of interactions. For example, in 3,5-Pyrazoledicarboxylic acid (CSD Ref. SEPNUX⁵¹, Fig. 5(d)), there are two carboxylic acid groups that have drastically different energy contributions – one that forms a doublet homosynthon and the other is without close contacts. In an extreme case (CSD Ref. CARCAZ⁵³, Fig. 5(f)), the carboxylic acid group is prevented from interacting due to the bulkiness of the overall molecule,

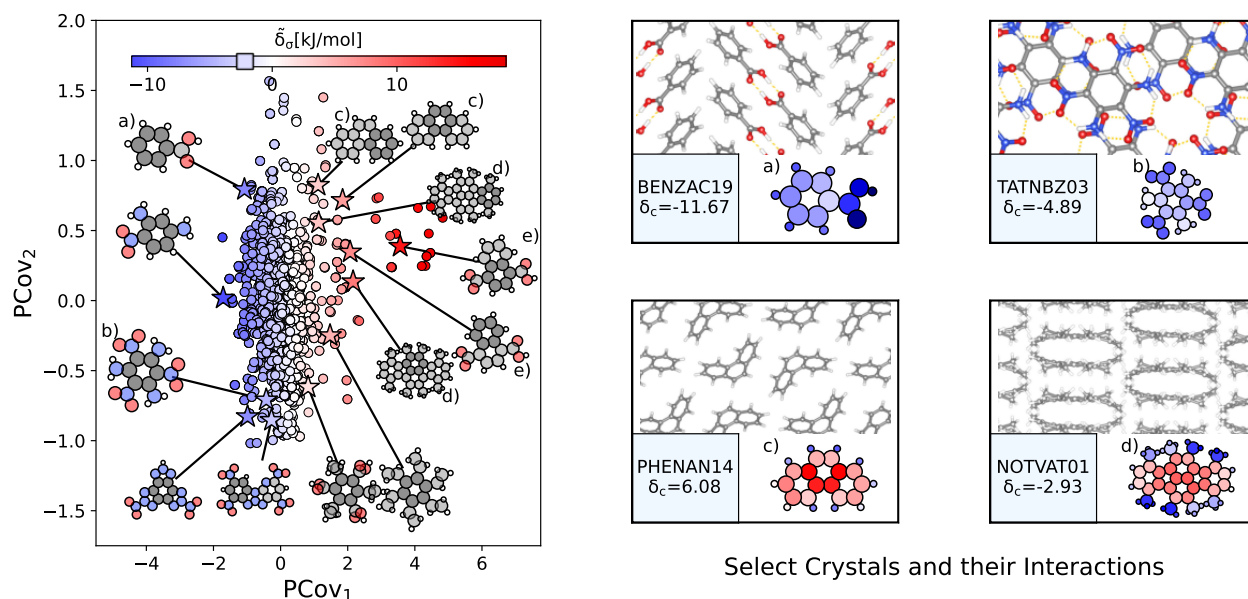


Fig. 6 The Interactions of Benzene-like Rings. (left) Principal Covariates Regression (PCovR) Map, where the color of each point denotes the estimated cohesive interaction of that motif and a marker on the color bar denotes the average value of benzene-like rings. The insets visualize several extremal or interesting motifs. (right) Select crystalline configurations and energy assignments: CSD Refs. (a) TATNBZ03⁵⁹, (b) BENZAC19⁶⁰, (c) PHENAN14⁶¹, and (d) NOTVAT01⁶². We also highlight the benzene-like motif from Fig. 5(f) in (e). In each panel on the right, the bottom row shows the total lattice energy of the crystal (in kJ/mol) and the corresponding molecules where the atoms have been recolored by their estimated lattice energy contribution (on the same scale as on the left panel).

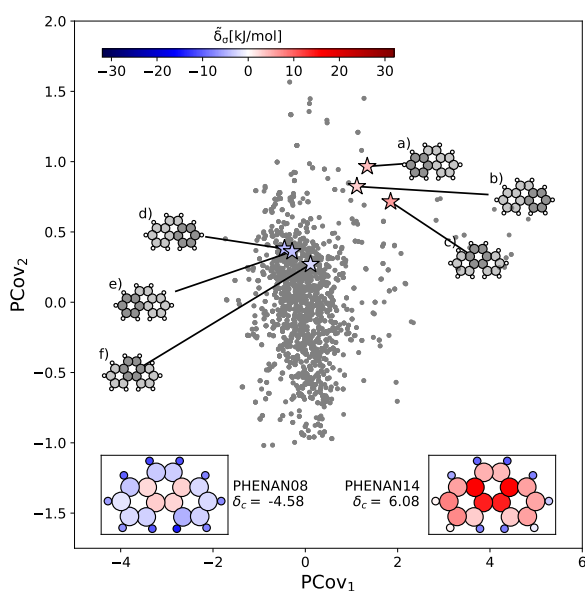


Fig. 7 Comparing the Motifs in Polymorphs of Phenanthrene. Here we project two distinct polymorphs of phenanthrene onto the PCovR map shown in Fig. 6. At ambient conditions, one polymorph is stable (PHENAN08⁶³), while the other is unstable (PHENAN14⁶¹, also shown in Fig. 6(c)). Looking at the same motifs in the unstable and stable phases, we see a shift leftwards as the motifs go from resisting crystallization to weakly binding. In the lower insets, we have recolored the atoms of the phenanthrene molecule based upon their contribution to the lattice energy in the different polymorphs. Note that the bicyclic carbon atoms, while no longer distorted, weakly resist crystallization, as they prevent the auxiliary hydrogens from more closely interacting with neighboring π bonds by distorting the molecule.

leading to a neutral contribution.

An interesting success of this energy assignment is the ability to identify stabilizing motifs in otherwise unstable or metastable crystals. This is the case for CSD Ref. NAPDCX⁵² (Fig. 5(e)), an unstable 1,4-Naphthalene-dicarboxylic acid that has an overall positive lattice energy at ambient pressure and temperature[‡]. Despite this instability, we can clearly identify a binding interaction between carboxylic acid groups.

3.2.3 6-Membered Unsaturated Carbon Rings

6-member unsaturated carbon rings (consistent with benzene molecules but more broadly-defined to include branched rings) show weak intermolecular interactions ranging from -11.27 kJ/mol to 18.75 kJ/mol, with the majority of interactions occurring in the -2.19 ± 3.0 kJ/mol range. Similar to Sec. 3.2.2, we generate a new PCovR using the averaged remnant descriptors and effective interactions using the 3'280 benzene-like motifs, as shown in the left panel of Fig. 6. Again, we have included a panel on the right showing the crystalline conformation and molecules colored by δ_c for select configurations.

The most strongly-binding benzene-like motifs occur in molecules where 1) the ring is functionalized by strongly interacting groups, 2) the interactions of these groups facilitate planar molecular geometry, and 3) stacking occurs between the benzene-like rings with these auxiliary groups. We see this in 2,4,6-trinitrobenzene-1,3,5-triamine (CSD Ref. TATNBZ03⁵⁹, Fig. 6(b)), where the aromatic carbon ring stacks above the pri-

[‡] Of the approximately 3'200 crystals studied in this article, only 23 have a positive lattice energy. This is covered in more detail in Appendix A3

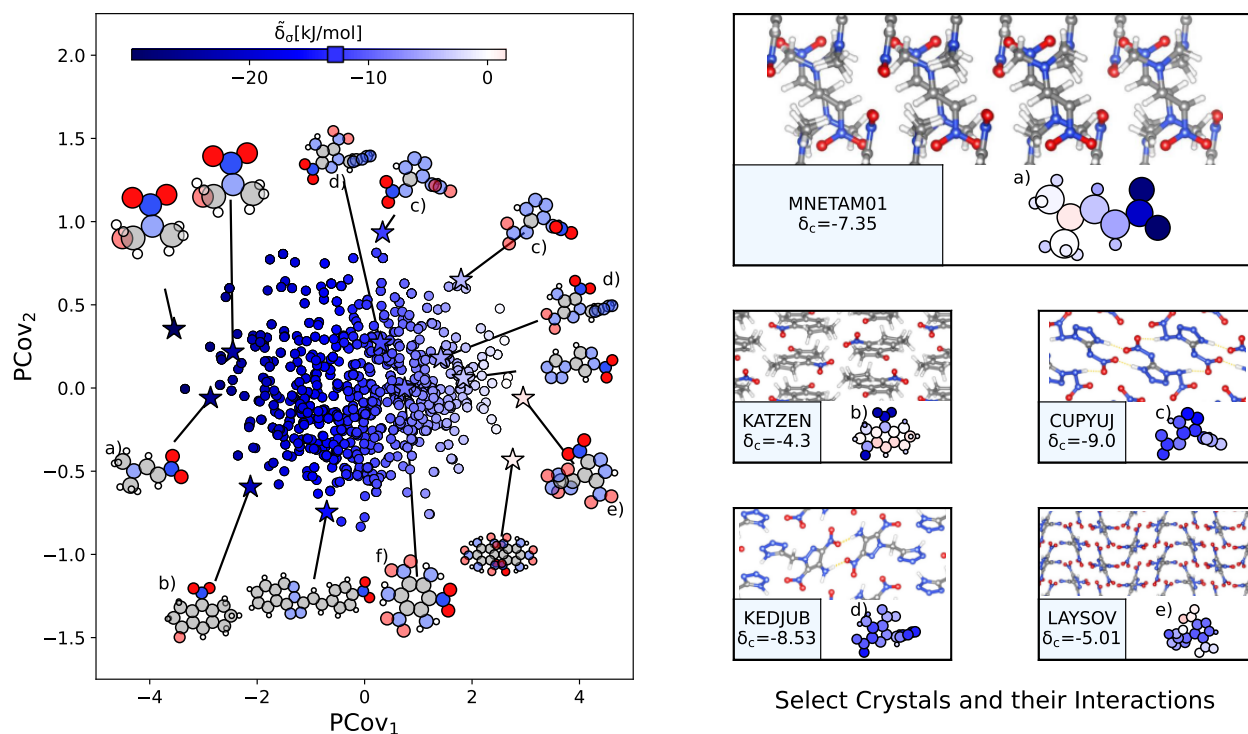


Fig. 8 The Interactions of Nitro Groups. (left) Principal Covariates Regression (PCovR) Map, where the color of each point denotes the estimated cohesive interaction of that motif. (right) Select crystalline configurations and energy assignments: CSD Refs. (a)TIJKEC⁶⁵, (b) KATZEN⁶⁶, (c) CUPYUJ⁶⁷, (d) KEDJUB⁶⁸, and (e) LAYSOV⁶⁹. We also highlight the nitro group of TATNBZ03⁵⁹ from Fig. 6(b) in (f). In each panel on the right, the bottom row shows the total lattice energy of the crystal (in kJ/mol) and the corresponding molecules where the atoms have been recolored by their estimated lattice energy contribution (on the same scale as on the left panel).

marily *intramolecular* nitro-amine interaction and in Fig. 6(a) (CSD Ref. BENZAC19⁶⁰), where they stack above the carboxylic acid homosynthon.

There are various reasons for weakly-binding benzene-like motifs, including weak stacking and steric hindrance. As is evident from Fig. 6(c-d), rings will *resist* crystallization when the interactions of the end groups lead to deformation of the ring geometry. Take for example phenanthrene (CSD Ref. PHENAN14⁶¹, Fig. 6(c)), a high-pressure polymorph that is unstable at ambient conditions (therefore has an overall positive lattice energy for the DFT reference used). Interestingly, we can pinpoint the localization of this deformation by looking at the atoms with the strongest positive contribution. While the keen reader may infer that this is solely due to the remnant descriptor reflecting the difference in strained and relaxed molecular geometry, we will note that a large difference in these representations can also coincide with a wealth of stabilizing intermolecular interactions, demonstrating that this simple linear model can differentiate molecular deformation from the introduction of new interactions.

This is further supported by comparing the motifs of this polymorph with its ambient-pressure, stable counterpart (CSD Ref. PHENAN08⁶³) to see how the nature of the same molecule changes based upon the interactions in the crystal. Both polymorphs adopt a similar herringbone crystal structure; however, the decreased molecular distortion and increased interactions between the auxiliary hydrogens and neighboring aromatic rings

in PHENAN08⁶³ results in a significantly lower lattice energy of $\delta_c = -4.58$. In Fig. 7, we project the motifs of PHENAN08⁶³ and PHENAN14⁶¹ onto our PCovR map from Fig. 6, we see this reflected by a left-shift of the motifs on the map, where the center ring moves from strongly resisting crystallization (Fig. 7(c)) to weakly interacting (Fig. 7(f)) and the periphery rings move from weakly resisting crystallization (Fig. 7(a,b)) to weakly binding (Fig. 7(e,f)). It is worth noting that PHENAN08⁶³ is an out-of-sample data point ($\epsilon = 0.2$ kJ/mol), demonstrating that the analysis in Fig. 6 is applicable beyond the initial reference set. We have included images of the PHENAN08⁶³ crystal configuration in Figure S5.

3.2.4 Nitro Groups

Nitro groups, defined as a nitrogen atom bonded to two terminal oxygen atoms, range in cohesive contributions from -29.9 kJ/mol to 1.56 kJ/mol, with most interaction strengths being -12.76 ± 5.66 kJ/mol. Similar to our previous examples, we generate a new PCovR using the averaged remnant descriptors and effective interactions of the 2'129 nitro groups, as shown in the left panel of Fig. 8. Again, we have included a panel on the right showing the crystalline conformation and constituent molecules colored by δ_a . Unlike carboxyl and benzene-like groups, the chemical diversity of nitro interactions is limited – this is either due to the chemical nature of nitro interactions or the availability of nitro-containing crystals in CSD.

The resonant or partial charge of the oxygen atoms leads to

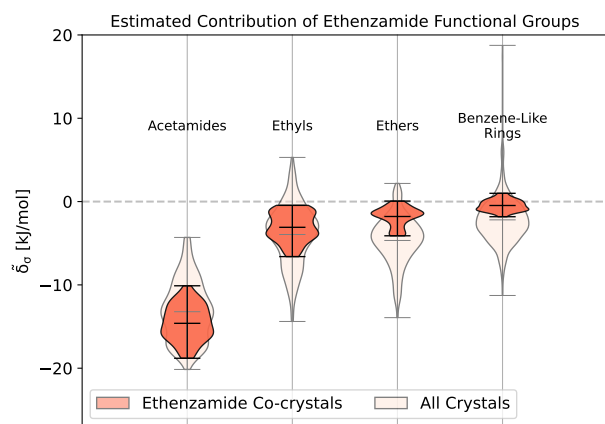


Fig. 9 Distribution of Energetic Contributions for the Functional Groups of Ethenzamide. Following the procedure outlined in 3.2, we have computed the estimated contribution to the binding energy $\bar{\delta}_{\sigma}$. Similar to Fig. 2, we have arranged the functional groups in order of average contribution, and the lines on each plot denote each group's extreme and mean contributions. Wider sections of the violin plot represent a higher probability that members of the population will take on the given value; the skinnier sections represent a lower probability. Here, darker sections refer to the distribution in the functional groups of the ethenzamide molecules, with lighter sections showing the distribution for the same functional group from Fig. 2.

strong binding in hydrogen-rich environments, supported by the results in Fig. 8. This is best typified by *trans*-*N,N*-Dimethyl-2-nitrovinylamine (CSD Ref. MNETAM01⁷⁰), a molecule where the nitro group is strongly interacting with the CH₃ end groups with some potential π -hole stacking⁷¹ between the nitrogen moieties, as shown in Fig. 8(a). The strength of these binding interactions lessens with the strength of the electron donors, with smaller contributions in crystals where the primary *O*...*H* interaction is with amine donors (e.g., Fig. 8(c, d), CSD Refs. CUPYUJ⁶⁷, KEDJUB⁶⁸). In some of these cases, the binding is likely weakened by intramolecular interactions, similar to the contributions of the nitro groups in 2,4,6-trinitrobenzene-1,3,5-triamine (CSD Ref. TATNBZ03⁵⁹, Fig. 8(f), seen earlier in Fig. 6(b)). Finally, to the right of the map, we see the strongest repulsive interactions from nitro groups in proximity to other nitro or aromatic nitrogen groups, such as the nitro-oxadiazole interaction in 3-(3,5-Dinitro-1*H*-pyrazol-4-yl)-4-nitro-1,2,5-oxadiazole (CSD Ref. LAYSOV⁶⁹, Fig. 8(f)).

3.3 A Case Study: Ethenzamide Co-crystals

We conclude by demonstrating how these models and methods can be used in the more practical context of crystal design. Ethenzamide is a common analgesic that has been the subject of numerous co-crystallization studies⁷²⁻⁸¹ due to the poor solubility of its homocrystalline form⁸². On the Cambridge Structure Database, there are currently 47 reported co-crystals of ethenzamide, of which there are 29 crystals that fit within the scope of this study and contain complete crystallographic information. The co-

forming molecules in these co-crystals are primarily hydrobenzoic acids, nitrobenzoic acids, and dicarboxylic acids, as well as a 3-toluic acid co-crystal⁷⁷ and two saccharin co-crystals⁸¹. A list of these crystals with their experimental and computed properties is given in Appendix A4.

We first compute the relaxed energies of the co-crystals and their molecular components, following the procedures outlined in Appendix A to obtain the reference geometries and binding energies of each crystal. For reference, our previous model built using Eq. (9) achieves an RMSE of 0.45kJ/mol and an MAE of 0.35kJ/mol more than sufficient to distinguish between the different categories of co-forming molecules, yet unable to provide any guidance in isomeric contexts (we have included a labeled parity plot in Figure S10). Following the procedure outlined in Appendix B, we identify the functional groups within the ethenzamide and estimate the contribution of their interactions to the molecular binding.

As shown in Fig. 9, most of the binding interactions unsurprisingly occur due to the acetamide group in the ethenzamide, with a 3.5kJ/mol difference between the weakest contributing acetamide motif and the most strongly contributing ethyl group, which is beyond the error in the overall model. From Fig. 9, we can also see that, while the ethyl and benzene-like rings behave similarly to other similar motifs across the entire dataset, the acetamide and ether groups are generally more and less stabilizing, respectively, than their counterparts at large. With the ether groups, this is reasonable – the geometry of the ether prevents much intermolecular interaction. With the acetamide group, this demonstrates that there is a large range of engineering that can happen to affect crystalline stability, which might be beneficial when considering molecular solubility.

From here, we use the PCovR of acetamide groups to identify other acetamide motifs that behave similarly, or dissimilarly, to those we see in the known ethenzamide co-crystals, as highlighted in Fig. 10. We first train our PCovR model on the acetamide groups in the training set, and project those from the ethenzamide dataset into the corresponding latent space. Because the interactions across the training set are much more diverse than within the ethenzamide set, we plot along the first and *third* covariate to show the best distinction between the two datasets[§]. We define similarity based upon the Euclidean distance in PCovR space – that is, acetamide groups that appear at a similar place on the map in Fig. 10. Note that because we compute the distance using all covariates, some points that seem extremal in Fig. 10 are not, as they are closer or further from the ethenzamide motifs in other dimensions.

We highlight the molecules that form the most similar acetamide networks to those in the ethenzamide dataset in Fig. 10 using an (o) marker and showing the molecule below. Those closest in PCovR space are molecules that form single acetamide homosynthons (e.g., Fig. 10(b,c), CSD Refs. MEGDOS⁸⁴ and LORMOV⁸⁵) or heterosynthons with a carboxylic acid group

[§] There is an interactive map of the first four covariates within our online repository at Cersonsky *et al.*⁴⁸

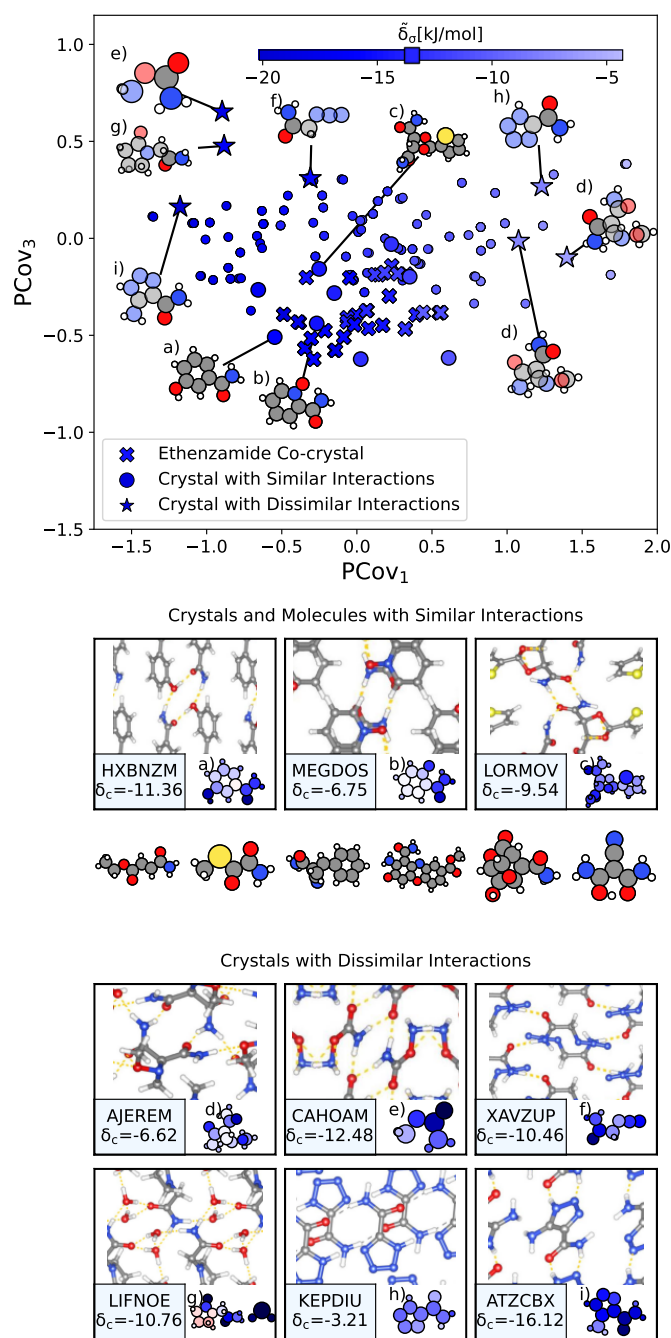


Fig. 10 The Interactions of Acetamide Groups. (top) Principal Covariates Regression (PCovR) Map, where the color of each point denotes the estimated cohesive interaction of that motif. Here we have plotted along the first and third covariates to best distinguish the acetamide groups of the known ethenzamide co-crystals from other groups. The markers correspond to: (x) known ethenzamide co-crystals, (o) crystals with similar acetamide interactions, and (*) crystals with dissimilar acetamide interactions. (middle) Crystals and molecules with similar acetamide interactions as those in the known ethenzamide co-crystals, including CSD Refs. (a) HXBNZM⁸³, (b) MEGDOS⁸⁴, and (c) LORMOV⁸⁵. (bottom) Crystals dissimilar acetamide interactions to the known ethenzamide co-crystals: CSD Refs. (d) AJEREM⁸⁶, (e) CAHOAM⁸⁷, (f) XAVZUP⁸⁸, (g) LIFNOE⁸⁹, (h) KEPDIU⁹⁰ and (i) ATZCBX⁹¹. Insets have been ordered from highest to lowest similarity to the interactions in the known ethenzamide co-crystals.

(e.g., Fig. 10(a), CSD Refs. HXBNZM⁸³).

Perhaps more interesting are the acetamide groups that form different network interactions, highlighted in the right panel in Fig. 10. These groups give insight into the other supramolecular synthons that form with ethenzamide across a range of stabilizing and destabilizing contributions. We see strong interactions in triazole-5-carboxaldehyde (Fig. 10(i), CSD Ref. ATZCBX⁹¹), where the acetamide group forms a heterosynthon with the triazole group, and in O-carbamoylhydroxylamine (Fig. 10(e), CSD Ref. CAHOAM⁸⁷), where the small size of the molecule facilitates both multiple homosynthon between acetamide groups as well as heterosynthon with the oxygen of the hydroxylamine groups. In 2-Oxopyrrolidineacetamide dihydrate (Fig. 10(g), CSD Ref. LIFNOE⁸⁹), a network of hydrogen bonds is formed between acetamide groups and water molecules. In azidoacetamide (Fig. 10(f), CSD Ref. XAVZUP⁸⁸), we see an acetamide homosynthon formed at an offset so that the azide group can stack directly above the NH...O interaction. We see weaker interactions in tetrazole-5-carboxamide (Fig. 10(h), CSD Ref. KEPDIU⁹⁰), where the acetamide group is interacting with the azole group, which, when compared with triazole-5-carboxaldehyde (Fig. 10(i)), demonstrates the range of acetamide-azole synthon binding. Finally, in 1-Methoxyaziridine-2,2-dicarboxamide (Fig. 10(d), CSD Ref. AJEREM⁸⁶), despite multiple acetamide interactions, we see a weakened acetamide network, likely due to the geometry of the molecule itself.

We do not suggest that these molecules could be used directly as co-formers; the train set was obtained with diversity as the primary goal, with no regard for availability, toxicity, ease of synthesis, or stability. Instead, each of these related and unrelated crystals gives insight into the types of interactions that may beget new ethenzamide co-crystals. The molecules shown in Fig. 10 can be used as inspiration to identify co-former candidates from libraries of biocompatible compounds and to guide future crystallization studies.

4 Conclusions

Molecular crystallization is a complex, multi-faceted process, that poses tremendous challenges to both quantitative modeling, and to the derivation of qualitative design principles. In this work we propose a data-driven strategy to build a database of the interaction motifs that are found in a diverse set of molecular crystals, to determine semi-quantitatively their contribution to the lattice energy, and to generate a library of molecular motifs that can be used to interpret the stability of known crystals and to assist the design of new ones.

In doing so, we have to strike a balance between several conflicting goals. By using a dataset that is constructed by selecting structures from the CSD while maximizing their structural diversity we ensure that we cover a broad range of chemical and packing motifs, while remaining focused on structures that are known to be experimentally realizable. By using a general-purpose, atom-centered structural representation that is capable of describing arbitrary structural correlations, we ensure that our data analysis is flexible and that it does not incorporate preconceived notions about molecular bonding. At the same time,

we ensure that the model focuses on the features that are most relevant to determine crystal stability by building a remnant descriptor that mimics the definition of the lattice energy as a difference between the total energies of the crystal and its constituents.

The resulting models achieve a respectable mean absolute error of about 0.4kJ/mol in predicting the atomic contributions to crystal stability using these descriptors that gives us a semi-quantitative estimate of the contribution of each atomic environment to the lattice energy and to compare between different co-crystals or between polymorphs that are stable at very different conditions. In order to translate these atomic contributions in a language that can be useful to crystal chemistry, we then assemble them to estimate the stabilizing power of traditional chemical groups (carboxylic acids, amines, ...) and build data-driven maps that facilitate the comparison of different chemical environments, by expressing the greatest amount of structural variability and simultaneously the best correlation with the lattice energy contribution. For each chemical moiety we provide an interactive map (on Materials Cloud⁴⁸) that allows to juxtapose different types of crystal environments, to identify structural patterns that are either stabilizing or destabilizing, and to contrast them with conventional motifs (e.g. hydrogen-bonding), demonstrated here for a few selected cases. With these tools, we aim to guide those designing molecular co-crystals in identifying suitable co-formers, which we demonstrate for the analgesic ethenzamide. As we demonstrate for phenanthrene, it is also possible to use these maps to compare polymorphs of the same molecule, and to analyze molecular motifs for a structure that is not part of our original reference set.

We hope that this library of molecular motifs will prove useful to applications to specific crystal-design problems. More broadly, we believe that the general ML protocol that we follow, combining regression of the ultimate target property with unsupervised analysis of molecular motifs, can inspire similar applications to the study of other classes of materials, ranging from metal and covalent organic frameworks to self-assembled monolayers and biological systems.

5 Author Contributions

RKC and MC designed the study and wrote the manuscript. RKC computed the molecular energies and geometries, built the machine learning models, and designed the figures. MP separated the crystals into molecular components, screened the dataset before relaxation calculations, started the molecular energy calculations, and edited the manuscript. EAE advised on the dataset provenance and curation and edited the manuscript.

6 Acknowledgments

This project was funded by NCCR Marvel Inspire Fellowship (MP), NCCR Marvel (RKC & MC), Trinity College (EAE), and ERC Grant 677013-HBMAP (RKC & MC).

The authors would like to acknowledge Federico Giberti, Andrea Anelli, and Guillaume Fraux for fruitful conversations at the study's start and culmination.

Conflicts of interest

There are no conflicts to declare.

Notes and references

- 1 M. A. E. Yousef and V. R. Vangala, *Crystal Growth & Design*, 2019, **19**, 7420–7438.
- 2 M. K. Dudek and K. Druzbecki, *CrystEngComm*, 2022, **24**, 1665–1678.
- 3 L. Iuzzolino, A. M. Reilly, P. McCabe and S. L. Price, *Journal of Chemical Theory and Computation*, 2017, **13**, 5163–5171.
- 4 S. Datta and D. J. W. Grant, *Nature Reviews Drug Discovery*, 2004, **3**, 42–57.
- 5 T. Beyer, G. M. Day and S. L. Price, *Journal of the American Chemical Society*, 2001, **123**, 5086–5094.
- 6 M. M. Azrain, M. R. Mansor, S. H. S. M. Fadzullah, G. Omar, D. Sivakumar, L. M. Lim and M. N. A. Nordin, *Synthetic Metals*, 2018, **235**, 160–175.
- 7 J. Mei, N. L. C. Leung, R. T. K. Kwok, J. W. Y. Lam and B. Z. Tang, *Chem. Rev.*, 2015, **115**, 11718–11940.
- 8 E. Krissinel and K. Henrick, *Journal of Molecular Biology*, 2007, **372**, 774–797.
- 9 Q. C. Zhang, D. Petrey, L. Deng, L. Qiang, Y. Shi, C. A. Thu, B. Bisikirska, C. Lefebvre, D. Accili, T. Hunter, T. Maniatis, A. Califano and B. Honig, *Nature*, 2012, **490**, 556+.
- 10 P. Ganguly and G. R. Desiraju, *CrystEngComm*, 2010, **12**, 817–833.
- 11 R. Davey, G. Dent, R. Mughal and S. Parveen, *Crystal Growth & Design*, 2006, **6**, 1788–1796.
- 12 A. Dey, M. T. Kirchner, V. R. Vangala, G. R. Desiraju, R. Mondal and J. A. Howard, *Journal of the American Chemical Society*, 2005, **127**, 10545–10559.
- 13 J. Sarma and G. R. Desiraju, *Crystal Growth & Design*, 2002, **2**, 93–100.
- 14 G. R. Desiraju, *Angew. Chem. Int. Ed.*, 2007, **46**, 8342–8356.
- 15 M. K. Corpinot and D.-K. Bucar, *Crystal Growth & Design*, 2019, **19**, 1426–1453.
- 16 I. J. Bruno, J. C. Cole, P. R. Edgington, M. Kessler, C. F. Macrae, P. McCabe, J. Pearson and R. Taylor, *Acta Cryst. B*, 2002, **58**, 389–397.
- 17 I. J. Bruno, J. C. Cole, M. Kessler, J. Luo, W. S. Motherwell, L. H. Purkis, B. R. Smith, R. Taylor, R. I. Cooper, S. E. Harris and others, *Journal of Chemical Information and Computer Sciences*, 2004, **44**, 2133–2144.
- 18 M. A. Neumann, F. J. Leusen and J. Kendrick, *Angewandte Chemie*, 2008, **120**, 2461–2464.
- 19 J. Hoja, H.-Y. Ko, M. A. Neumann, R. Car, R. A. DiStasio and A. Tkatchenko, *Science Advances*, 2019, **5**, eaau3338.
- 20 M. A. Spackman and D. Jayatilaka, *CrystEngComm*, 2009, **11**, 19–32.
- 21 M. A. Spackman and J. J. McKinnon, *CrystEngComm*, 2002, **4**, 378–392.
- 22 O. Egorova, R. Hafizi, D. C. Woods and G. M. Day, *The Journal of Physical Chemistry A*, 2020, **124**, 8065–8078.

- 23 F. Musil, S. De, J. Yang, J. E. Campbell, G. M. Day and M. Ceriotti, *Chem. Sci.*, 2018, **9**, 1289–1300.
- 24 S. Wengert, G. Csányi, K. Reuter and J. T. Margraf, *J. Chem. Theory Comput.*, 2022, **18**, 4586–4593.
- 25 S. Wengert, G. Csányi, K. Reuter and J. T. Margraf, *Chem. Sci.*, 2021, **12**, 4536–4546.
- 26 V. Kapil and E. A. Engel, *Proceedings of the National Academy of Sciences*, 2022, **119**, e2111769119.
- 27 A. Seko, H. Hayashi, K. Nakayama, A. Takahashi and I. Tanaka, *Physical Review B*, 2017, **95**, 144110.
- 28 T. Bereau, D. Andrienko and O. A. von Lilienfeld, *Journal of Chemical Theory and Computation*, 2015, **11**, 3225–3233.
- 29 M. Cordova, E. A. Engel, A. Stefaniuk, F. Paruzzo, A. Hofstetter, M. Ceriotti and L. Emsley, *The Journal of Physical Chemistry C*, 2022, **126**, 16710–16720.
- 30 Britts, K. and Karle, I.L., *Acta Crystallographica [1948-1967]*, 1967, **22**, 308.
- 31 L. Talirz, S. Kumbhar, E. Passaro, A. V. Yakutovich, V. Granata, F. Gargiulo, M. Borelli, M. Uhrin, S. P. Huber, S. Zoupanos, C. S. Adorf, C. W. Andersen, O. Schütt, C. A. Pignedoli, D. Passerone, J. VandeVondele, T. C. Schulthess, B. Smit, G. Pizzi and N. Marzari, *Scientific Data*, 2020, **7**,.
- 32 M. J. Willatt, F. Musil and M. Ceriotti, *The Journal of Chemical Physics*, 2019, **150**, 154110.
- 33 F. Pedregosa, G. Varoquaux, A. Gramfort, V. Michel, B. Thirion, O. Grisel, M. Blondel, P. Prettenhofer, R. Weiss, V. Dubourg, J. Vanderplas, A. Passos, D. Cournapeau, M. Brucher, M. Perrot and E. Duchesnay, *Journal of Machine Learning Research*, 2011, **12**, 2825–2830.
- 34 G. Imbalzano, A. Anelli, D. Giofré, S. Klees, J. Behler and M. Ceriotti, *The Journal of chemical physics*, 2018, **24**, 241730.
- 35 R. K. Cersonsky, B. A. Helfrecht, E. A. Engel, S. Kliavinek and M. Ceriotti, *Mach. Learn.: Sci. Technol.*, 2021, **2**, 035038.
- 36 B. A. Helfrecht, R. Semino, G. Pireddu, S. M. Auerbach and M. Ceriotti, *The Journal of Chemical Physics*, 2019, **151**, 154112.
- 37 C. Ben Mahmoud, A. Anelli, G. Csányi and M. Ceriotti, *Physical Review B*, 2020, **102**, 235130.
- 38 SMARTS: A Language for Describing Molecular Patterns, 1997, daylight.com/dayhtml/doc/theory/theory.smarts.html.
- 39 RDKit: Open-source cheminformatics., <https://www.rdkit.org>.
- 40 S. De Jong and H. A. Kiers, *Chemometrics and Intelligent Lab. Sys.*, 1992, **14**, 155–164.
- 41 B. A. Helfrecht, R. K. Cersonsky, G. Fraux and M. Ceriotti, *Machine Learning: Science and Technology*, 2020, **1**, 045021.
- 42 Janeda, S. and Mootz, D., *Zeitschrift fur Naturforschung, B: Chemical Sciences*, 1998, **53**, 1197.
- 43 Janeda, S. and Mootz, D., *Zeitschrift fur Naturforschung, B: Chemical Sciences*, 1999, **54**, 103.
- 44 Mootz, D. and Staben, D., *Zeitschrift fur Naturforschung, B: Chemical Sciences*, 1993, **48**, 1325.
- 45 M. Schreyer, L. Guo, S. Thirunahari, F. Gao, M. Garland, *Journal of Applied Crystallography*, 2014, **47**, 659.
- 46 Klapotke, T.M. and Kurz, M.Q. and Scharf, R. and Schmid, P.C. and Stierstorfer, J. and Suceška, M., *ChemPlusChem*, 2015, **80**, 97.
- 47 Sarlauskas, J., *Proceedings of the Seminar on New Trends in Research of Energetic Materials*, 2014, **17**, 1005.
- 48 R. K. Cersonsky, M. Pakhnova, E. A. Engel and M. Ceriotti, *Lattice Energies for a Diverse Set of Molecular Crystals*, 2022.
- 49 A. Briceno, D. Leal, G. Ortega, G. D. de Delgado, E. Ocando, L. Cubillan, *CrystEngComm*, 2013, **15**, 2795.
- 50 Gardon, M. and Pinheiro, C.B. and Chapuis, G., *Acta Crystallographica, Section B: Structural Science [1983-2012]*, 2003, **59**, 527.
- 51 Roussel, P. and Bentiss, F. and Drache, M. and Conflant, P. and Lagrenee, M. and Wignacourt, J.-P., *Journal of Molecular Structure*, 2006, **798**, 134.
- 52 Derissen, J.L. and Timmermans, C. and Schoone, J.C., *Crystal Structure Communications*, 1979, **8**, 533.
- 53 Chen, T.K. and Ales, D.C. and Baenziger, N.C. and Wiemer, D.F., *Journal of Organic Chemistry*, 1983, **48**, 3525.
- 54 M. C. Etter, *Accounts of Chemical Research*, 1990, **23**, 120–126.
- 55 M. C. Etter, *The Journal of Physical Chemistry*, 1991, **95**, 4601–4610.
- 56 P. Vishweshwar, A. Nangia and V. M. Lynch, *The Journal of Organic Chemistry*, 2002, **67**, 556–565.
- 57 T. R. Shattock, K. K. Arora, P. Vishweshwar and M. J. Zaworotko, *Crystal Growth & Design*, 2008, **8**, 4533–4545.
- 58 P. Chen, Z. Zhang, S. Parkin, P. Zhou, K. Cheng, C. Li, F. Yu and S. Long, *Royal Society of Chemistry Advances*, 2016, **6**, 81101–81109.
- 59 Zhijie Chua, and Gianopoulos, C.G. and Zarychta, B. and Zhurova, E.A. and Zhurov, V.V. and Alan Pinkerton, A., *Crystal Growth and Design*, 2017, **17**, 5200.
- 60 Weizhao Cai, and Katrusiak, A., *CrystEngComm*, 2012, **14**, 4420.
- 61 Fabbiani, F.P.A. and Allan, D.R. and David, W.I.F. and Moggach, S.A. and Parsons, S. and Pulham, C.R., *CrystEngComm*, 2004, **6**, 504.
- 62 Sygula, A. and Fronczek, F.R. and Rabideau, P.W., *Tetrahedron Letters*, 1997, **38**, 5095.
- 63 Petricek, V. and Cisarova, I. and Hummel, L. and Kroupa, J. and Brezina, B., *Acta Crystallographica, Section B: Structural Science [1983-2012]*, 1990, **46**, 830.
- 64 L. Leiserowitz, *Acta Cryst. B*, 1976, **32**, 775–802.
- 65 Vasiliev, A.D. and Astachov, A.M. and Kekin, Yu.V. and Kruglyakova, L.A. and Stepanov, R.S., *Acta Crystallographica, Section C: Crystal Structure Communications [1983-2014]*, 2001, **57**, 1192.
- 66 Salla, M. and Butler, M.S. and Ruby Pelingon, and Kaeslin, G. and Croker, D.E. and Reid, J.C. and Jong Min Baek, and Bernhardt, P.V. and Gillam, E.M.J. and Cooper, M.A. and Robertson, A.A.B., *ACS Medicinal Chemistry Letters*, 2016, **7**, 1034.
- 67 Fischer, D. and Klapotke, T.M. and Stierstorfer, J., *Angewandte Chemie, International Edition*, 2015, **54**, 10299.

Journal of the Chemical Society Perkin Transactions 2 [1972-2002], 1974, 1849.

Supplementary Information: A data-driven interpretation of the stability of organic molecular crystals

Rose K. Cersonsky,^{*a} Maria Pakhnova,^a Edgar A. Engel,^b and Michele Ceriotti^a

A Constructing the Datasets

A.1 Dataset Curation

We start with a dataset containing approximately 10'600 ground-state, geometry-optimized configurations originally used for training (10'000) and testing (604) a model for predicting NMR chemical shieldings for organic molecular crystals¹. These molecular crystals contain 14 of the most common chemical species, and their energies have already been computed using the protocol described in Sec. A.2. For our study, we selected all H, C, N, O, and S-containing molecular crystals composed of non-polymeric, neutrally-charged molecules and less than 200 atoms per unit cell. This resulted in 2'707 and 551 such crystals for training and testing, corresponding to 3'242 and 628 molecules, respectively. A similar screening protocol was applied to the ethenzamide co-crystals summarized in Appendix A.4. All data and workflows were managed by the *signac* and *signac-flow* packages^{2,3}.

Reducing to H, C, N, O, S First, we eliminated all structures containing chemical species other than H, C, N, O, and S. We have limited our dataset to these species to maximize the diversity of our dataset while minimizing the size of our SOAP representation (the length scales with $\mathcal{O}(n_{species}^2)$). This resulted in the largest reduction of the overall dataset, from roughly 10'000 to 3'800 crystals.

Separating the Crystals We then separated each crystal into its molecular constituents. First, we computed radial distribution functions, combining the data from all structures in a single histogram for each pair of chemical species. We determined the cutoff distance for covalent bonds as the first near-zero minimum after the first neighbor peak. We computed a supercell consisting of 3^3 - 7^3 repeat unit cells for each crystal to screen for polymers.

Determining the Set of Unique Molecules Finally, we determined the irreducible set of constituent molecules by identifying identical/redundant molecules based on the similarity of their SOAP features. In practice, a similarity kernel $K_{mm'} = \mathbf{x}_m \cdot \mathbf{x}_{m'}$ was constructed by computing the similarity of each pair of molecules m and m' and iteratively removing molecules $m' > m$, for which $K_{mm'} > \epsilon$. For the later step of identifying the molecular motifs, we were careful to index the location of each atom in the original crystal within the constituent molecules. .

Eliminating Charged Molecules We computed the molecular charges from density-functional tight-binding (DFTB) calculations, using the DFTB+ package⁴ and the Third-Order Parameterization for Organic and Biological Systems (3OB)^{5,6} to perform a Γ -point calculation for each crystal structure. Structures containing molecules carrying an absolute charge greater than 0.5e were eliminated. We also eliminated those crystals with common zwitterionic moieties such as NH_3^+ or COO^- . These steps ensure that *for the given dataset* the lattice energies are defined unequivocally.

A.2 Relaxing Molecular Geometries

Quantum-Espresso Parameterization To ensure that the resultant geometries and energies are consistent and comparable to those obtained for the crystal structures in Cordova *et al.*¹, the geometry optimizations for the molecules were performed using the same computational parameters using Quantum Espresso⁷. These parameters were as follows: the PBE exchange-correlation functional⁸, the D2 dispersion correction⁹, ultrasoft pseudopotentials with GIPAW reconstruction^{10,11}, and an equivalent plane-wave energy cutoff of 60 Ryd. We converged the energies within 1E-4 Ryd and forces below 1E-3 Ryd/Bohr, respectively. Furthermore, we compute the binding energy based on the lowest energy conformer represented in the dataset, ensuring comparability between crystals and co-crystals of similar stoichiometries without needing to obtain the global minimum conformation of each molecule.

Simulation Boxes for Molecules *in vacuo* To determine the simulation boxes appropriate to describe the molecules *in vacuo*, we performed Γ -point calculations. We converged the results with respect to the size of the simulation cell and, *e.g.*, the

^a Laboratory of Computational Science and Modeling (COSMO), École Polytechnique Fédérale de Lausanne, Lausanne, Switzerland

^b TCM Group, Trinity College, Cambridge University, Cambridge, UK

* Present address: Rose.Cersonsky@wisc.edu

separation between the periodic images of the molecules. Based on calculations using a variety of simulation cell sizes for 20 different molecules, we determined a minimum vacuum padding of 2-4 times the largest dimension of the molecule proved sufficient to converge the resultant molecular energies. We confirmed these results against those obtained using Martyna-Tuckerman electrostatic decoupling¹².

A.3 Properties of the Resulting Dataset

Properties of the resulting dataset are given in Fig. S1, with an inset denoting the correlation of a given property with the error in regressing the lattice energy (ϵ_δ) given the best-performing model reported in the text. Red curves and lines denote the testing set, and black curves and lines are the training set.

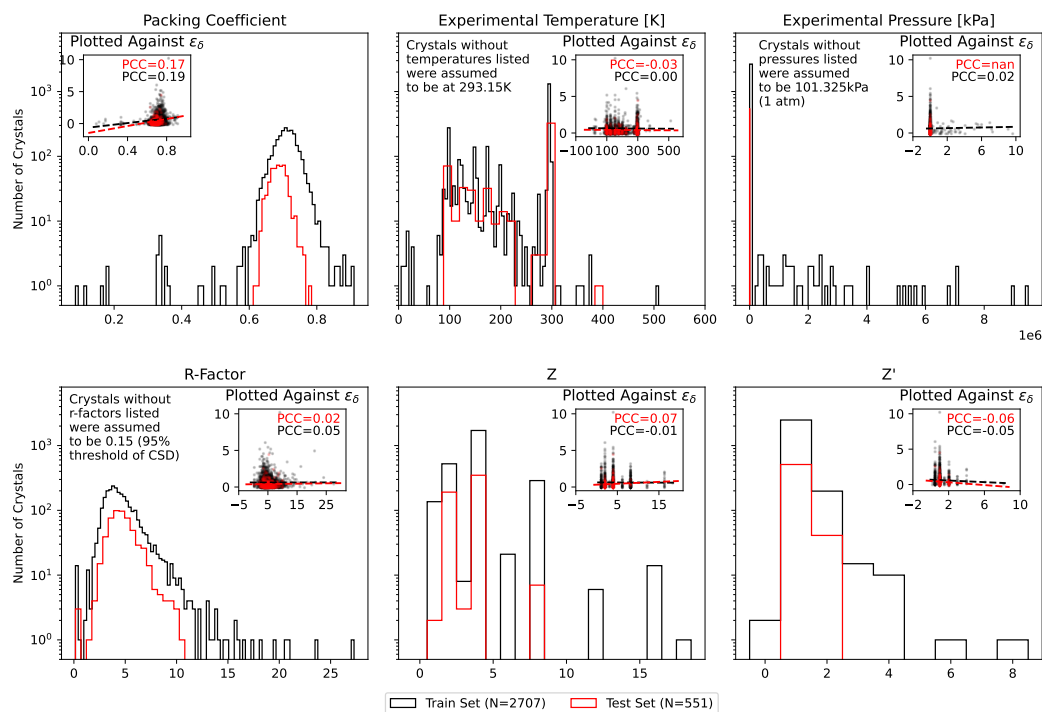


Fig. S1 Analysis of the structures contained in this dataset. In each panel, we show the histogram of a structural parameter across the training set (black) and testing set (red). For parameters not reported in the original data entry, we have assumed ambient conditions, as noted in each panel. In the insets, we show the relationship between these parameters and the error in regressing the binding energy using the remnant model described in the text, ϵ_δ to show that there is the relationship between these parameters and the regression performance.

Of the 3'258 total crystals, 23 (0.7%) are shown to be unstable (e.g., $\Delta_c > 0$) for the reference DFT method at ambient conditions. The majority of these are structures were experimentally determined at high pressure (CSD Refs. VOFVAN23¹³, JAYDUI06¹⁴, PHENAN14¹⁵), low temperature (HAMFEJ¹⁶, ZZZEU05¹⁷, EHAJUS¹⁸, NTSALA¹⁹, ZAQFAB²⁰, IDUWEJ²¹, UWUFAV²², UVOMIC²³, LAGMUC²⁴, GAFYES²⁵, PUYVAG²⁶, NUZGOG²⁷, NSBTOA²⁸), or have high r-factors (QNACRD03²⁹). From visual analysis, the remaining six crystals (LINJUN³⁰, XOSBIS³¹, TETYOH³², DBANQU³³, NAPDCX³⁴, and DUPLUV³⁵) appear to have kinetically trapped molecular components, with a large difference between the crystalized molecular geometry and the dilute gas molecular geometry. This can be due to many reasons, but we reason that this is due to small strains induced by the reported lattice parameters, as computing the variable cell relaxations results in a marginally different crystal that has a negative lattice energy.

Table S1 Summary of Crystals with $\delta_c > 0$

	n_c	δ_c [kJ/mol]	Packing Coeff.	R-Factor [%]	Exp. Temp. [K]	Exp. Press. [GPa]	Z	Z'
VOFVAN23 ¹³	52	0.0430	0.7760	7.45	295.	1.	2	1
HAMFEJ ¹⁶	68	0.2930	0.7440	3.87	100.	–	4	1
ZZZEEU05 ¹⁷	68	0.3180	0.7580	7.89	20.	–	4	1
LINJUN ³⁰	68	0.3990	0.7380	4.10	–	–	4	1
EHAJUS ¹⁸	30	0.4420	0.7450	3.18	150.	–	2	0
XOSBIS ³¹	60	0.4580	0.7190	2.90	296.	–	4	1
NTSALA ¹⁹	68	1.1170	0.7520	4.90	108.15	–	4	1
ZAQFAB ²⁰	72	2.0340	0.7090	7.15	123.	–	4	1
TETYOH ³²	80	2.1780	0.7020	4.84	293.	–	4	2
IDUWEJ ²¹	30	3.4640	0.72	4.40	123.20	–	2	0
JAYDUI06 ¹⁴	44	3.4890	0.8570	7.64	295.	5.93	4	1
UWUFAV ²²	104	3.7560	0.7650	11.39	100.	–	4	1
DBANQU ³³	144	3.8130	0.75	9.65	–	–	4	1
NAPDCX ³⁴	48	3.8580	0.7580	8.20	–	–	2	1
UVOMIC ²³	60	4.0790	0.7770	5.43	125.	–	1	0
LAGMUC ²⁴	16	4.2590	0.7330	2.02	100.	–	2	0
DUPLUV ³⁵	132	4.8510	0.7410	4.20	–	–	4	1
GAFYES ²⁵	112	5.67	0.7440	5.88	150.	–	4	1
PUYVAG ²⁶	14	5.9990	0.7290	4.90	173.	–	1	0
PHENAN14 ¹⁵	96	6.0820	0.7540	11.30	293.	0.70	4	1
NUZGOG ²⁷	16	8.4160	0.7430	4.26	100.	–	1	0
QNACRD03 ²⁹	72	9.2720	0.7550	20.60	–	–	2	1
NSBTOA ²⁸	80	20.9550	0.8150	9.	153.15	–	4	1

A.4 Ethenzamide Co-Crystals

For our case study later in the text, we have curated a set of ethenzamide co-crystals from the Cambridge Structure Database, as summarized in Table S2. We have screened and computed energies using the exact protocols as in A.1 - A.2.

Table S2 Summary of Ethenzamide Co-crystals

	Co-former	n_c	E_c [Ryd]	δ_c [kJ/mol]	Packing Coeff.	R-Factor [%]	Exp. Temp. [K]	Z	Z'
VAKTOS ³⁶	Ethylmalonic Acid	80	-920.76	-6.74	0.69	4.58	110.0	2	1
ORIKOR ³⁷	2-NBA	80	-1015.04	-5.98	0.69	6.19	296.0	2	1
VAKTOS01 ³⁶	Ethylmalonic Acid	160	-1841.51	-6.71	0.68	9.62	110.0	4	1
JIFHAK ³⁸	2,4 DHBA	160	-1922.96	-6.13	0.65	5.47	296.0	4	1
REHSUU ³⁹	4-hydroxybenzoic Acid	156	-1756.28	-6.32	0.72	5.98	110.0	4	1
QULLUF ⁴⁰	Gentisic Acid (2,5 DHBA)	160	-1922.94	-6.41	0.7	7.63	110.0	4	2
REHTAB ³⁹	Fumaric Acid	58	-671.35	-6.78	0.69	7.63	110.0	2	1
ORILAE ³⁷	2,4-DNBA	168	-2470.77	-7.43	0.69	4.03	296.0	4	1
WUZJUX ⁴¹	3,5 DNBA	84	-1235.34	-5.97	0.63	8.04	110.0	2	1
VUHFIO01 ⁴²	Saccharin	160	-2129.21	-6.18	0.69	5.95	110.0	4	1
VUHFIO ⁴²	Saccharin	80	-1064.59	-5.91	0.71	3.81	110.0	2	1
WUZJEH ⁴¹	3,5 DNBA, Dioxane	98	-1373.7	-5.97	0.72	7.4	160.0	2	1
WUZJOR ⁴¹	3,5 DNBA	84	-1235.33	-5.87	0.61	6.26	110.0	2	1
QULLUF02 ⁴⁰	Gentisic Acid (2,5 DHBA)	160	-1922.9	-6.06	0.72	6.19	110.0	4	1
ODIDEN01 ⁴³	3,5 DHBA and H2O	160	-2152.0	-8.86	0.7	6.62	296.0	2	1
WUZHOP ⁴¹	3,5 DNBA	168	-2470.72	-6.32	0.72	5.44	110.0	4	1
ORIKIL ³⁷	Gallic acid	128	-1499.15	-6.49	0.65	3.82	296.0	2	1
TIWPIB ⁴⁴	Glutaric Acid	160	-1841.74	-8.03	0.67	4.88	293.0	4	1
WUZKAE ⁴¹	3,5 DNBA	84	-1235.34	-5.97	0.64	6.34	110.0	2	1
REHSAA ³⁹	Salicylic Acid	156	-1756.29	-5.74	0.71	7.31	100.0	4	1
WUZJIL ⁴¹	3,5 DNBA, Dioxane	98	-1373.7	-5.98	0.72	5.69	110.0	2	1
ODICUC ⁴⁵	2,4 DHBA	160	-1922.93	-5.95	0.69	4.49	296.0	4	1
QULLUF01 ⁴⁰	Gentisic Acid (2,5 DHBA)	160	-1922.94	-6.43	0.7	12.33	110.0	4	1
WUZKEI ⁴¹	3,5 DNBA	84	-1235.33	-5.9	0.63	5.47	110.0	2	1
ORILEI ³⁷	3-toluic acid	164	-1644.76	-5.53	0.67	3.91	296.0	4	1
REHSII ³⁹	Vanillic Acid	172	-1977.88	-6.04	0.7	7.37	193.0	4	1
ORIKUX ³⁷	3-NBA	160	-2030.17	-6.03	0.69	5.42	296.0	4	1
FENQEX ⁴³	Gentisic Acid (2,5 DHBA)	160	-1922.94	-6.41	0.7	4.9	296.0	4	2
WUZHOP01 ⁴¹	3,5 DNBA	84	-1235.34	-5.92	0.72	7.62	110.0	2	1

B Methods

B.1 SOAP Hyperparameters

SOAP descriptors were generated using the Librascal library⁴⁶ (commit 6f7a4002) using the following hyperparameters:

- max_radial: 8
- max_angular: 4
- interaction_cutoff: 7.0
- gaussian_sigma_constant: 0.3
- cutoff_smooth_width: 0.5
- soap_type: "PowerSpectrum"
- gaussian_sigma_type: "Constant"
- radial_basis: "GTO"
- cutoff_function_type: "RadialScaling"
- cutoff_function_parameters: {rate: 1.5, exp: 3.0, scale: 2.0}

As tuning these hypers could favor one representation over another, we chose cutoff and scaling parameters to be consistent with the chemical geometry, noting that changing these parameters within this range has minimal effect on the errors. We determined the number of radial and angular channels (corresponding to the "resolution" of the descriptors) by balancing the number of features in each feature vector with the in-sample error of δ_c . The resulting SOAP vectors included 3-body correlations for each atomic neighborhood up to 7Å, weighting neighbor contributions with a radial scaling procedure introduced in Willatt *et al.*⁴⁷.

B.2 Filtering the Environmental Contributions

As noted in the main text, we applied a filtering scheme to the estimated contributions of each atomic environment. This technique reduces the number of extreme contributions attributed to any given environment, as shown in the changes in distribution in Fig. S2.

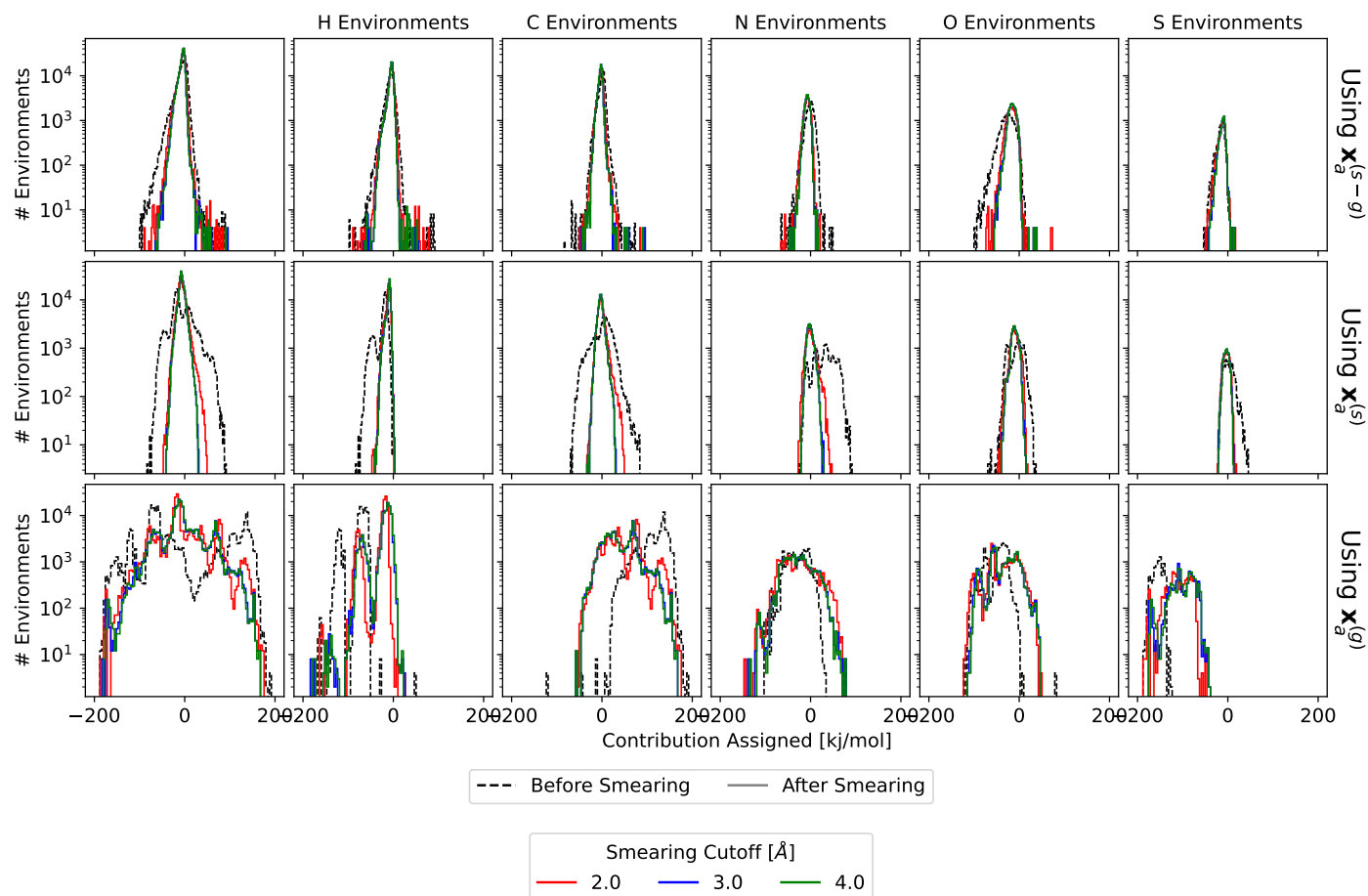


Fig. S2 Effect of “Smearing” the Contributions using Eq. (11). Note that $x_c^{(s-g)}$ yields the most stable result, compared to $x_c^{(s)}$ and $x_c^{(g)}$.

Notice that all of these vary based on representation and environment. In most cases, we see the distribution narrow with the smearing – signifying a regularization to the estimated contributions (e.g., dampening of extreme values). The smearing converges to a constant set of contributions with an increasing smearing cutoff, typically 2.0-3.0 Å (we use 2.0Å for all results in the text).

B.3 Identifying Molecular Motifs

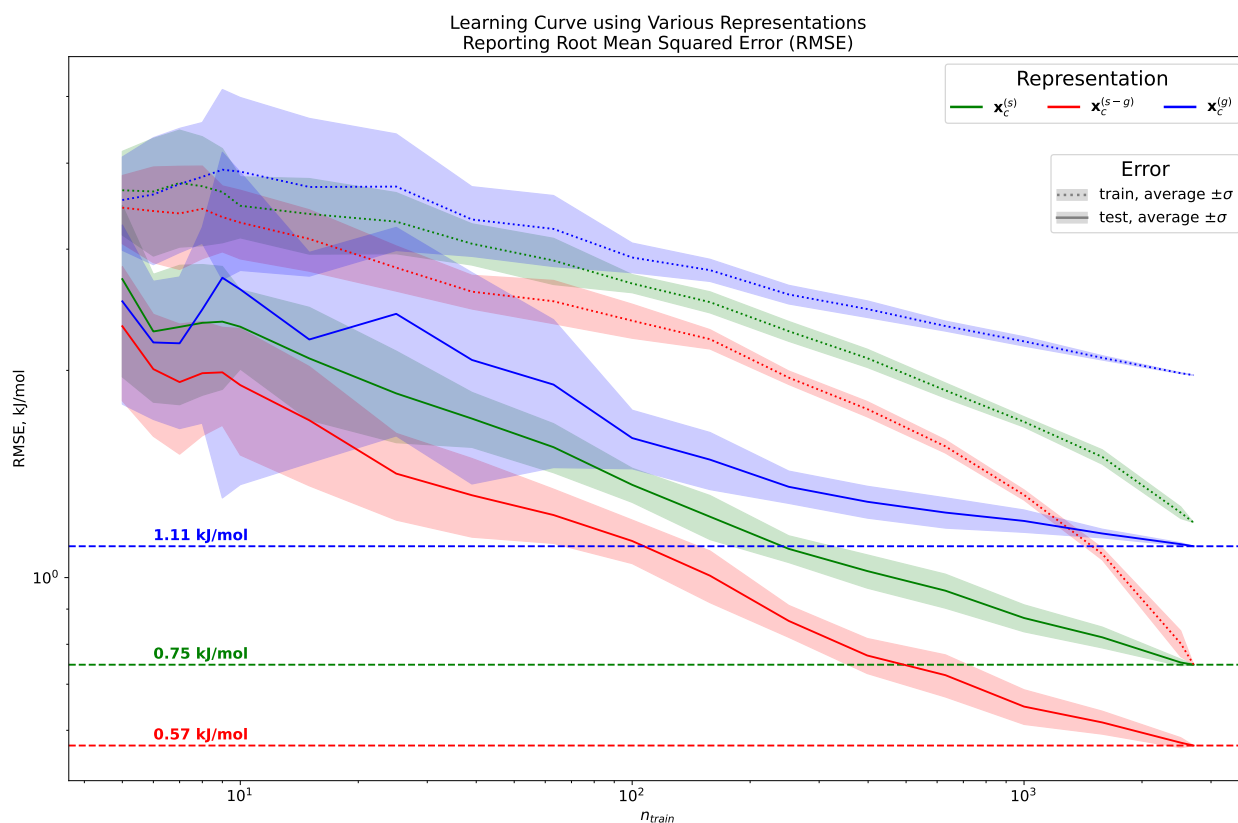
We employed RDKit Substructure Matching⁴⁸ to identify the molecular motifs. For this, we took (our typical) .xyz format of the molecular geometries and converted them to .mol format using the openbabel software⁴⁹. When labeling each collection of atoms, we assign each fragment its most specific designation, e.g., each nitro group was not also considered as two nitroso groups. We used the SMARTS strings⁵⁰ listed in Table S3 to identify motifs in the molecules.

	Name	SMARTS String	# Instances
Sulfur-Based	Disulfide	[#6]~[#16;X2]~[#16;X2]~[#6]	256
	Dithiole	s1~s~c~c~c1, s1~c~s~c~c1	138
	Sulfide Chain	[#16]~[#16;X2]~[#16;X2]~[#16]	200
	Sulfonamide	[SX3] (~[OX1]) (~[#6])~[#7]	7
	Sulfinyl	[!#8]~[#16;X3] (~[!#8])~[OX1]	190
	Sulfonate Esters	[SX4] (~[OX1]) (~[OX1]) ([#6])~[O;X2,-]	58
	Sulfonyl	[!#8]~[#16;X4] (~[OX1]) (~[!#8])~[OX1]	545
	Thiazole	s1~n~c~c~c1, s1~c~n~c~c1	163
	Thiazolidine	S1~N~C~C~C1, S1~C~N~C~C1	138
	Thiocarbonyl	C~[SX1]	359
	Thiocarboxamide	[#1,#6]~C(~[SX1])[#7]	176
	Thiodiazole	s1~n~c~n~c1, s1~c~n~n~c1, s1~n~n~c~c1, s1~n~c~c~n1	289
	Thioether	[#6]~[SX2]~[#6]	1920
	Thioketone	[#6]~[#6] (~[S;X1]) [#6]	42
	Thiol	[#6;!\$(C=,[!#6])] [SX2H]	54
	Thiophene	s1~c~c~c~c1	516
	Thiourea	[#7]~C(~[SX1])[#7]	318
Nitrogen-Based	Aryl Amines	[N\$(N-c);H1,H2;r0]	1209
	Carbonyls	[#6,#7,#1]~[C!\$(C;X3] (~[#8])~[#8])] (~[#6,#8,#1])~[O;X1]	1549
	3° Amines	[#7;X3;H0] ([#6]) ([#6]) [#6]	1859
	2° Amines	[#7;X3;H1] ([#6]) [#6]	1504
	1° Amines	[#7;X3;H2] [#6]	752
	Acetamide	[#7;X3;r0;H2]~[#6;X3;H0]~[O;X1]	342
	Azide	[#7;X2]~[#7;X2]~[#7;X1]	266
	Azo	[#6]-N=N-[#6]	115
	Carbamide	[#7;X3]~C(~[O;X1])~[#7;X3]	399
	Diazine	n1~n~c~c~c~c1, n1~c~n~c~c~c1, n1~c~c~n~c~c1	758
	Hydrazine	[#7;X3]~[#7;X3;H2]	414
	Hydroxyl- amines	[#6]~[#7;X3] (~[#6])~[#8;H1]	92
	Imidazole	n1~c~n~c~c1	444
	Isoxazole	o1~n~c~c~c1, o1~c~n~c~c1	78
	Nitrile	[#6]~[#7;X1]	68
	Nitro	[#8;X1]~[#7]~[#8;X1]	2129
	Nitroso	[#7]~[#8;X1]	498
	Oxidiazole	o1~n~c~n~c1, o1~c~n~n~c1, o1~n~n~c~c1, o1~n~c~c~n1	344
	Oxime	[#6]~[#7;X2]~[#8;H1]	285
	Pentazole	n1~n~n~n~n1	4
	Pyrazole	n1~n~c~c~c1	458
	Pyridine	n1~c~c~c~c~c1	574
	Pyrrole	n1~c~c~c~c1	219
Tetrazine	n1~n~n~n~c~c1, n1~n~c~n~n~c1	74	
Tetrazole	n1~c~n~n~n1	630	
Triazine	n1~n~n~c~c~c1, n1~n~c~n~c~c1, n1~c~n~c~n~c1	285	
Triazole	n1~n~n~c~c1, n1~c~n~n~c1	657	
Oxygen-Based	Carboxyls	[O;X1]~C~[O;H1]	1023
	Alcohols	[#6!\$([#6]=O)]~[O;H1]	2603
	Carbonate	[#8;X2]~[C] (~[#8;X1])~[#8;X2]	54
	Epoxide	O1CC1	252
	Ester	C(~[O;X1])~[O;H0;X2]~[C]	1218
	Ether	[#8;X2] (~[C;r0])~[#6]	736
	Furan	o1~c~c~c~c1	256
	Ketone	[#6] [CX3] (~[O;X1]) [#6]	1041
	Peroxides	[#8;X2]~[O;X2]	77
	Water	[OH2]	868
Carbon-Based	Alkane	[C;H2,H3]~[C;H2,H3]	4784
	Alkene	[C;H1,H0]=[C;H1,H0]	2413
	Alkyne	[C]#[C;H1]	8
	Benzene-like Rings	c1ccccc1	3280
	Ethyl	[C;H2;X4]~[C;H3;X4]	709
	Methyl	[C;H3;X4]	5313

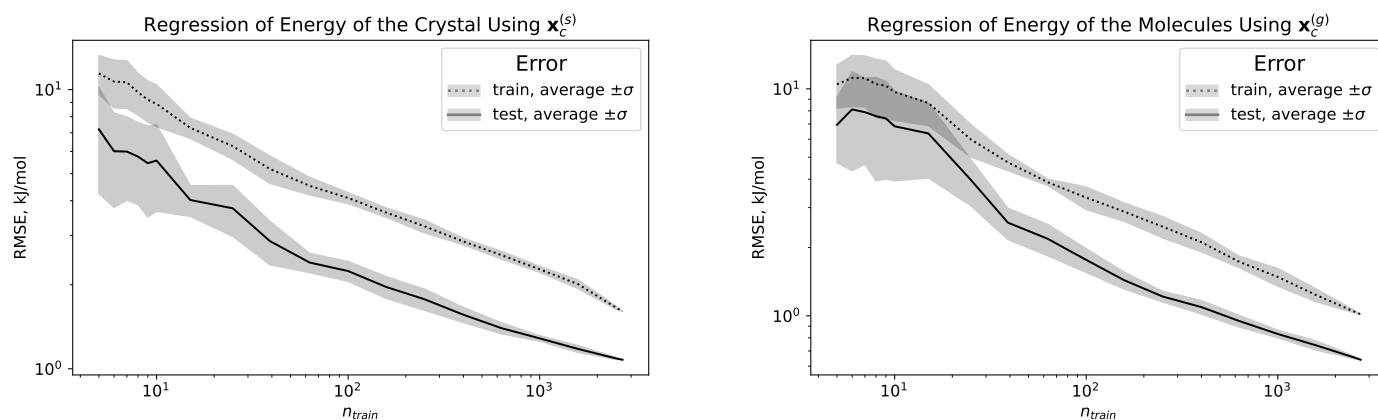
Table S3 Table of SMARTS Strings used to Identify Molecular Motifs. Notice that some SMARTS strings deviate from typical convention in order to accommodate the translation from thermodynamic coordinates (.xyz) to molecular connectivity graph format (.mol), as well as to define certain groups as mutually exclusive.

C Additional Results and Visualizations

C.1 Learning Curves



(a) Learning Curve of Various Representations on δ_c .



(b) Learning Curve of $\mathbf{x}_c^{(s)}$ on e_c .

(c) Learning Curve of $\mathbf{x}_m^{(g)}$ on e_m .

Fig. S3 Learning curves for lattice energy for the various representations used in this study. We varied the ratio of mutually-exclusive and randomly-selected training and testing points in each learning curve and conducted a regularized ridge regression. For each ratio, we conducted ten trials with random training sets and report the average (line) and standard deviations (shaded area).

For each descriptor, we constructed learning curves to demonstrate the saturation (or lack thereof) of the regression model on lattice energy. Each learning curve was run using `scikit-learn.model_selection.learning_curve` using a 10-fold cross-validation on a regularized ridge regression pulling randomly from our established training set. All learning curves demonstrate that we are still within a small-data regime (noted by the absence of saturation), justifying our focus on simple and data-efficient linear models.

C.2 Kernel Ridge Regression Models

Kernel Type	Structure-Wise Definition $K_{AB} = \frac{1}{n_A n_B} \sum_{a,b} \dots$	Equivalent RKHS Definition $K =$
Crystal Environments	$k(\mathbf{x}_a^{(s)}, \mathbf{x}_b^{(s)})$	$\phi_c^{(s)} (\phi_{c'}^{(s)})^T$
Molecular Environments	$k(\mathbf{x}_a^{(g)}, \mathbf{x}_b^{(g)})$	$\phi_c^{(g)} (\phi_{c'}^{(g)})^T$
Remnant of the RKHS Features	$k(\mathbf{x}_a^{(s)}, \mathbf{x}_b^{(s)}) + k(\mathbf{x}_a^{(g)}, \mathbf{x}_b^{(g)})$ $- k(\mathbf{x}_a^{(s)}, \mathbf{x}_b^{(g)}) - k(\mathbf{x}_a^{(g)}, \mathbf{x}_b^{(s)})$	$\left[(\phi_c^{(s)} - \phi_c^{(g)}) (\phi_{c'}^{(s)} - \phi_{c'}^{(g)})^T \right]$
Remnant Environments	$k(\mathbf{x}_a^{(s-g)}, \mathbf{x}_b^{(s-g)})$	$\phi_c^{(s-g)} (\phi_{c'}^{(s-g)})^T$

Table S4 Equations for Non-linear Kernels We computed regressions using the given kernel equations for crystals A and B and their corresponding atoms a and b . Mercer’s theorem ensures that for a positive-definite kernel on x , there exists a non-linear mapping $x \mapsto \phi$ such that $K = \phi\phi^T$, for which we have included our notation.

We computed regressions with both (i) an optimized RBF kernel (with optimal γ found by employing a subset of 1,000 crystals taken from the training set and (ii) a parameter-free cosine kernel. We ran kernel ridge regression models using `scikit-learn.linear_model.KernelRidge`⁵¹ employing a 90/10 training / validation split. The results on the offset test set are given in Table S5.

Regression Equation	RBF Kernel		Cosine Kernel	
	RMSE	MAE	RMSE	MAE
$\mathbf{e}_c = \phi_c^{(s)} (\phi_{c'}^{(s)})^T \mathbf{w}_c$	0.904	0.665	1.039	0.772
$\mathbf{e}_m = \phi_m^{(g)} (\phi_{m'}^{(g)})^T \mathbf{w}_m$	0.392	0.294	0.496	0.373
$\delta_c = \left[\phi_c^{(s)} (\phi_{c'}^{(s)})^T \right] \mathbf{w}_c$ $- \sum_{m \in \mathcal{C}} \frac{n_m}{n_c} \left(\left[\phi_m^{(g)} (\phi_{m'}^{(g)})^T \right] \mathbf{w}_m \right)$	0.913	0.681	1.061	0.805
$\delta_c = \phi_c^{(s)} (\phi_{c'}^{(s)})^T \mathbf{w}$	0.694	0.508	0.742	0.526
$\delta_c = \phi_c^{(g)} (\phi_{c'}^{(g)})^T \mathbf{w}$	1.097	0.714	1.097	0.71
$\delta_c = (\phi_c^{(s)} - \phi_c^{(g)}) (\phi_{c'}^{(s)} - \phi_{c'}^{(g)})^T \mathbf{w}$	0.541	0.403	0.589	0.425
$\delta_c = \phi_c^{(s-g)} (\phi_{c'}^{(s-g)})^T \mathbf{w}$	0.515	0.382	0.66	0.489

Table S5 Results of Kernel Ridge Regression Exercises. We have written each equation using reproducing kernel hilbert space (RKHS) notation (see Table S4), denoting the training set with $'$. Note the difference between the bottom entries, which represent (1) the “remnant version of non-linear feature vectors ϕ and (2) the non-linear mapping of the remnant vector employed in the main text. In each kernel regression, an independent, 2-fold cross-validated model was built on our 2’707 crystal training set in an 80/20 train/validation split. Here we report the RMSE and MAE (in kJ/mol) on a separate testing set of 551 crystals (or the coinciding 628 molecules). Each regression equation \mathbf{w} is unique to that regression.

C.3 Expanded Violin Plot

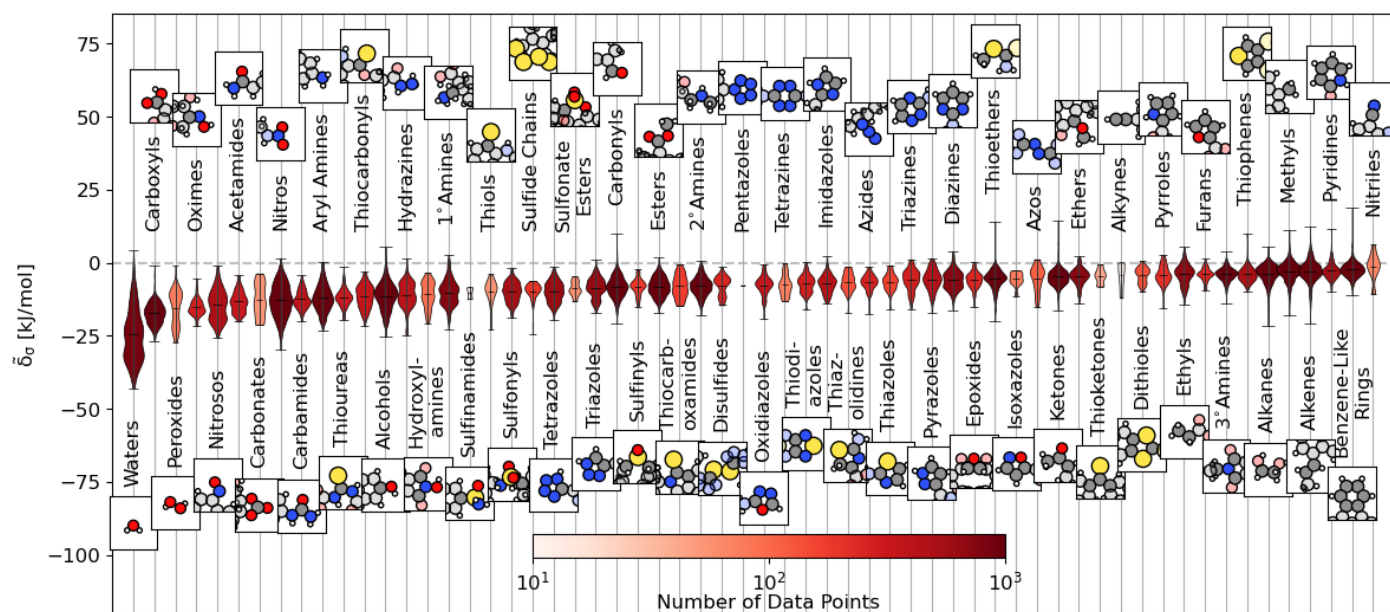
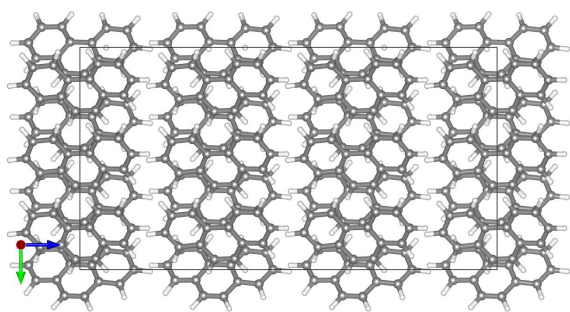
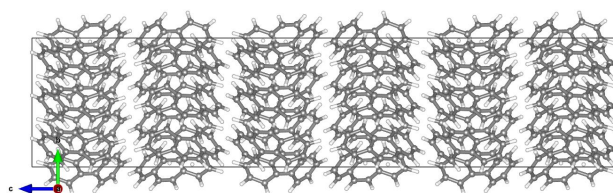


Fig. S4 Violin Plot from Fig. 2, expanded to include all functional groups. A representative example is shown above or below the violin plot with the functional group highlighted for each functional group. The lines on each plot denote each group's extrema and mean contributions. The plots colors reflect the number of examples within the dataset, ranging from 4 (pentazole) to 5313 (methyl groups)

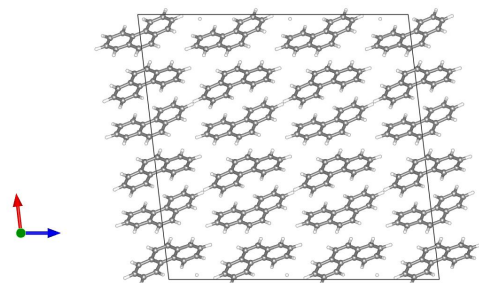
C.4 Images of Phenanthrene Polymorphs



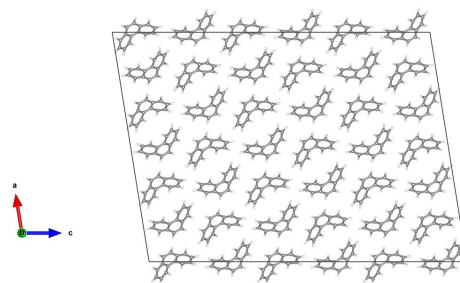
(a) View of PHENAN08⁵² along *a* axis.



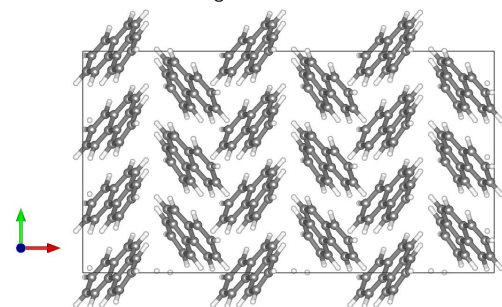
(b) View of PHENAN14¹⁵ along *a* axis.



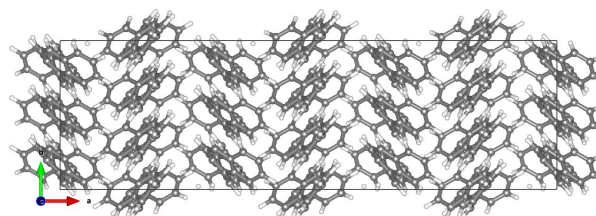
(c) View of PHENAN08⁵² along *b* axis.



(d) View of PHENAN14¹⁵ along *b* axis.



(e) View of PHENAN08⁵² along *c* axis.



(f) View of PHENAN14¹⁵ along *c* axis.

Fig. S5 Axial views of the stable (a, c, e) and unstable (b, d, f) phenanthrene polymorphs. 3x3x3 supercells are shown to include all intermolecular interactions.

C.5 Additional PCovR Maps

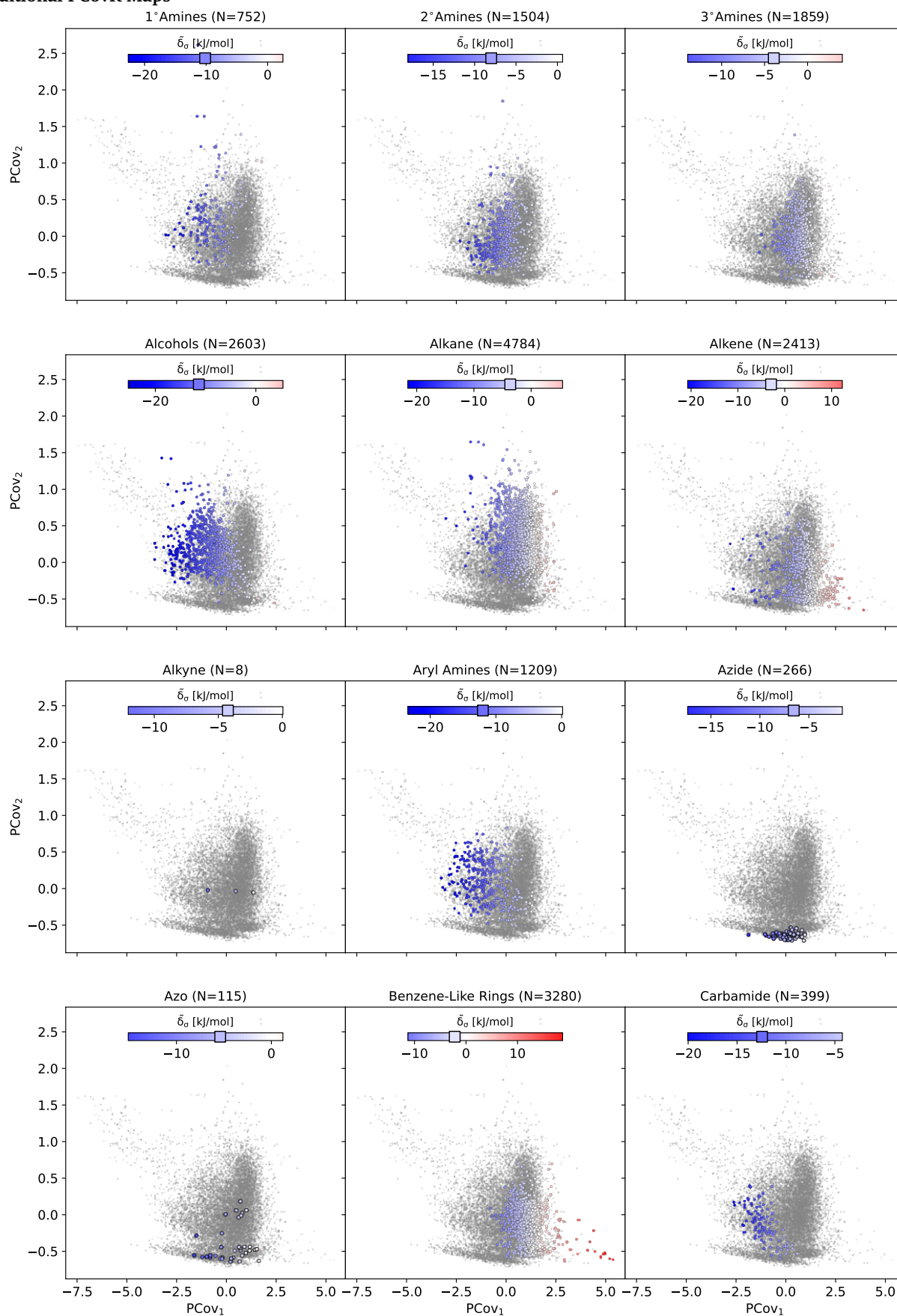


Fig. S6 PCovR map from Fig. 3, highlighting each type of functional group. Each map is on the same color scale; however, we have truncated the color bar to demonstrate the range of cohesive interactions. We have denoted the average of all group members by a square marker on the color bar.

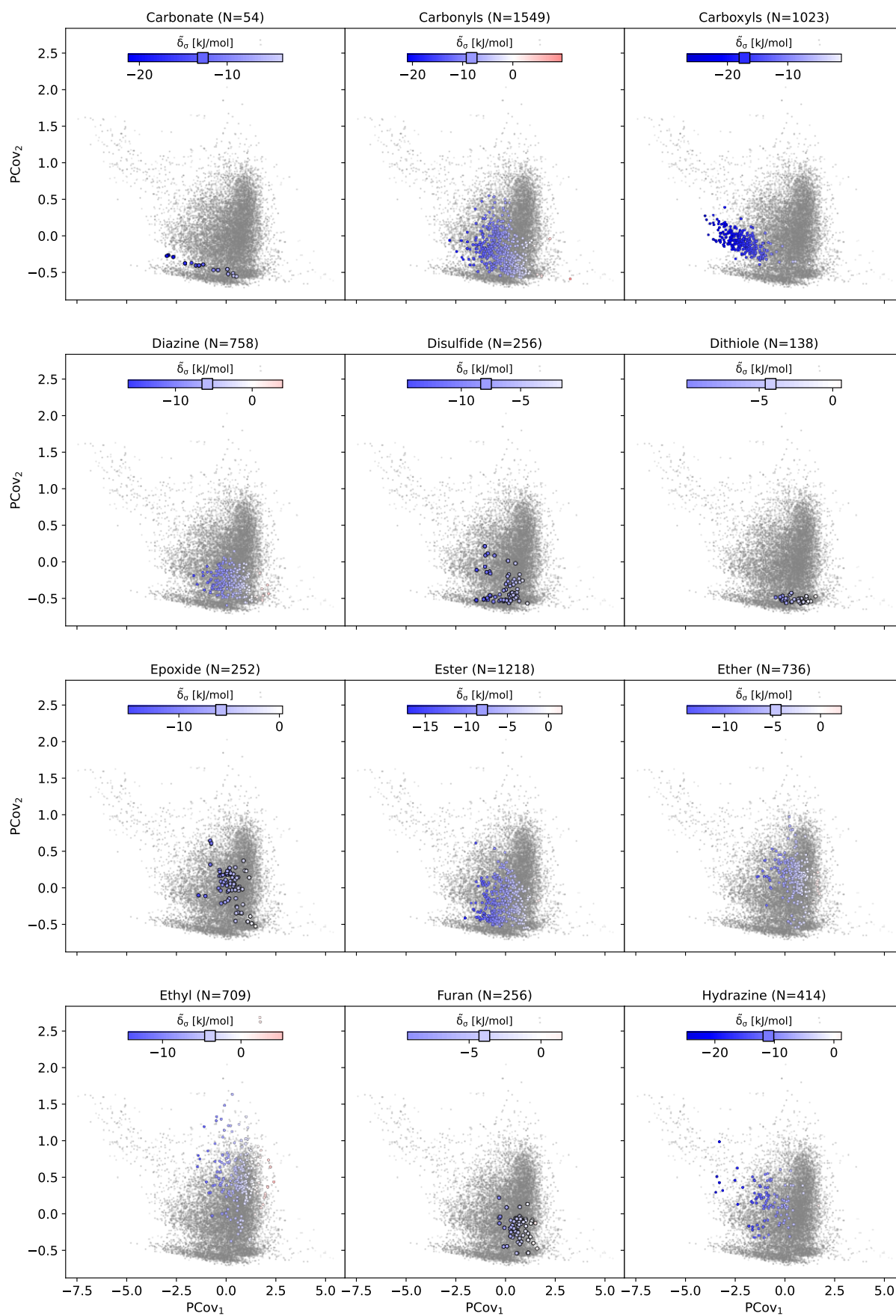


Fig. S7 PCovR map from Fig. 3, highlighting each type of functional group. Each map is on the same color scale; however, we have truncated the color bar to demonstrate the range of cohesive interactions. We have denoted the average of all group members by a square marker on the color bar.

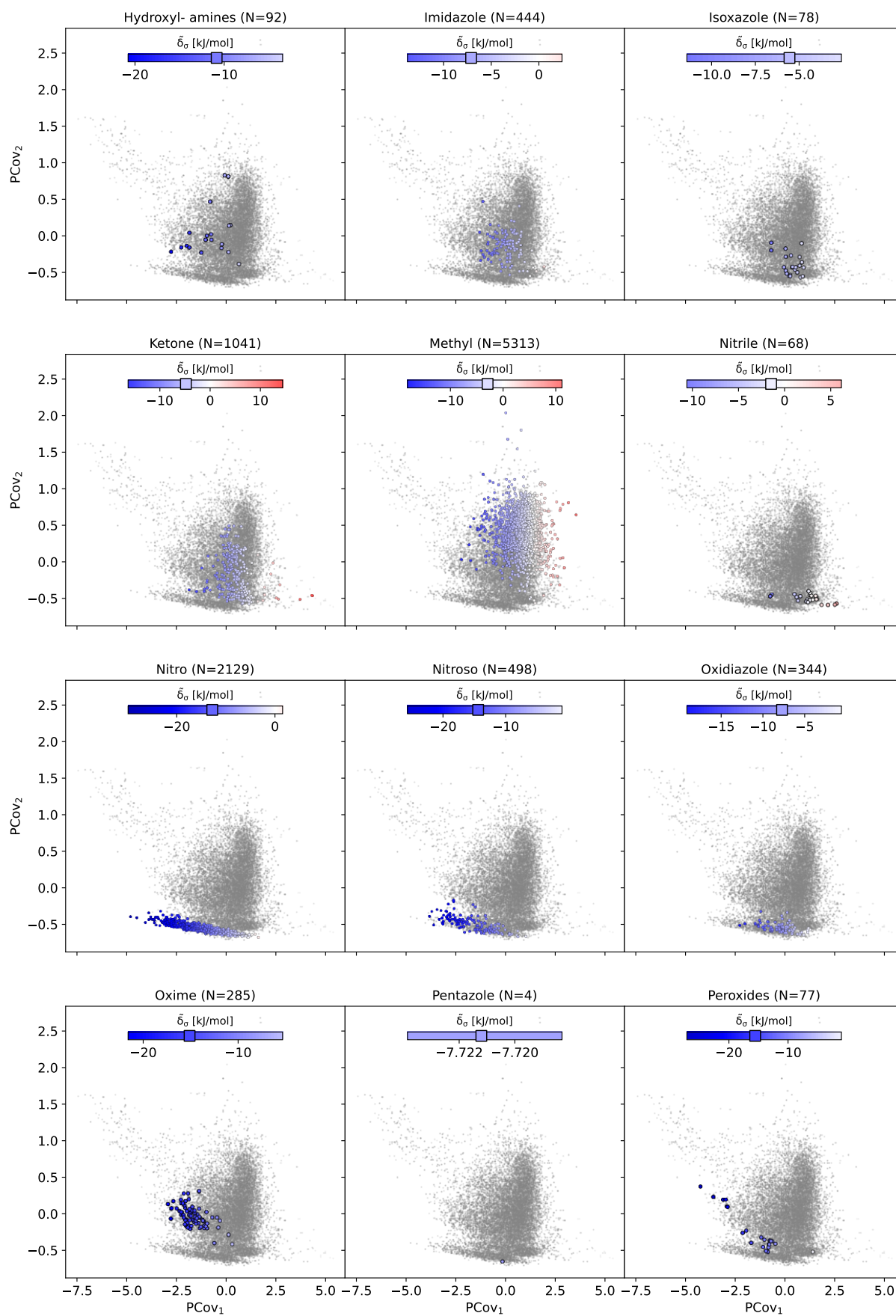


Fig. S8 PCovR map from Fig. 3, highlighting each type of functional group. Each map is on the same color scale; however, we have truncated the color bar to demonstrate the range of cohesive interactions. We have denoted the average of all group members by a square marker on the color bar.

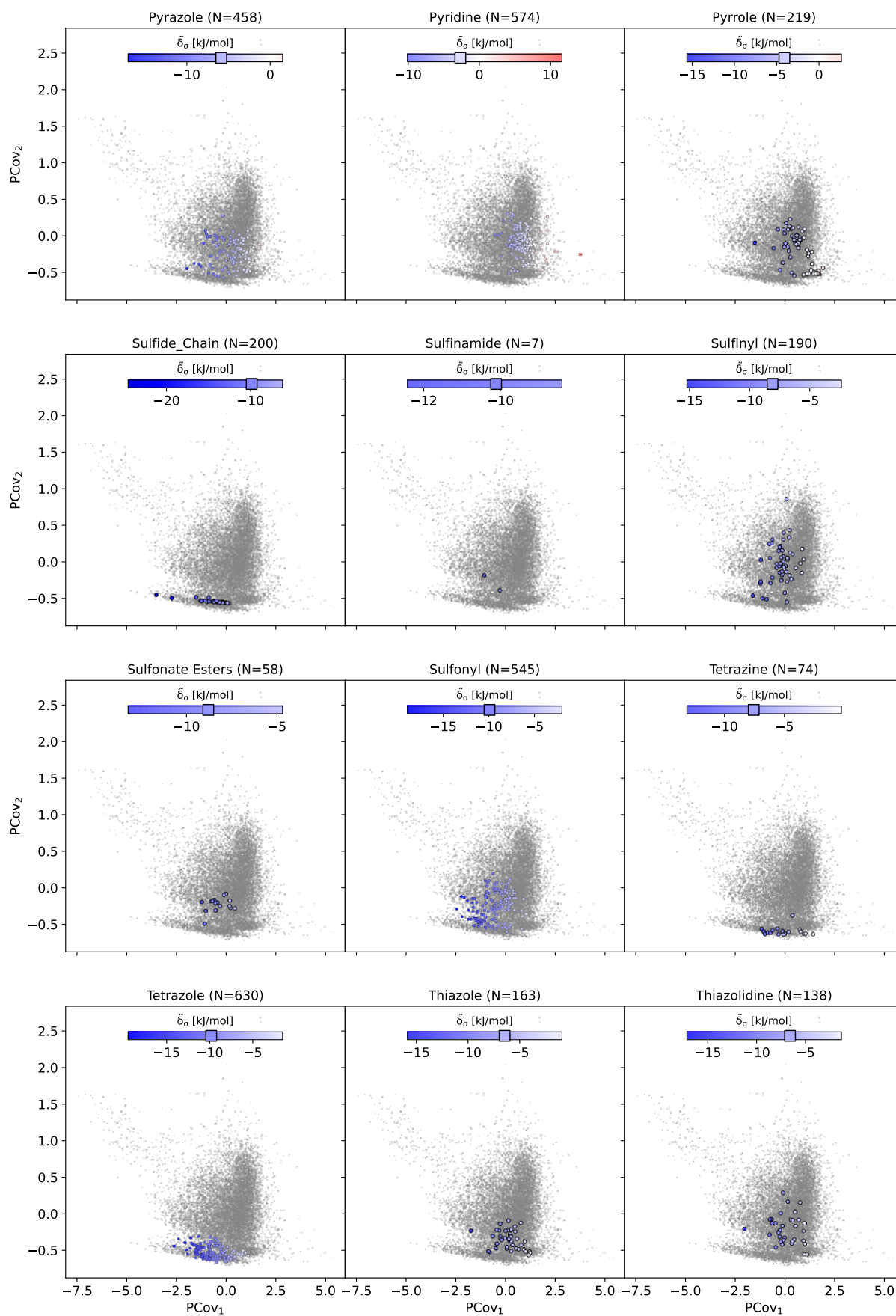


Fig. S9 PCovR map from Fig. 3, highlighting each type of functional group. Each map is on the same color scale; however, we have truncated the color bar to demonstrate the range of cohesive interactions. We have denoted the average of all group members by a square marker on the color bar.

C.6 Parity Plot for Ethenzamide Dataset

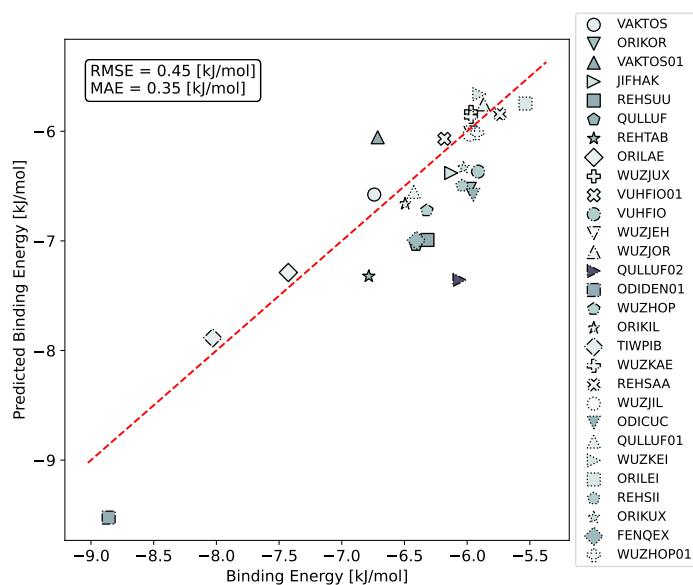


Fig. S10 Parity plot showing regression errors for the 29 ethenzamide co-crystals. Regressions were computed using the regularized ridge regression trained the remnant descriptor $x_c^{(s-g)}$ of the 2'707 training set crystals. Here we have labeled each point by its corresponding CSD refcode.

Notes and references

- 1 M. Cordova, E. A. Engel, A. Stefaniuk, F. Paruzzo, A. Hofstetter, M. Ceriotti and L. Emsley, *The Journal of Physical Chemistry C*, 2022, **126**, 16710–16720.
- 2 C. S. Adorf, V. Ramasubramani, B. D. Dice, M. M. Henry, P. M. Dodd and S. C. Glotzer, *glotzerlab/signac*, 2019, <https://doi.org/10.5281/zenodo.2581326>.
- 3 C. S. Adorf, P. M. Dodd, V. Ramasubramani and S. C. Glotzer, *Computational Materials Science*, 2018, **146**, 220–229.
- 4 B. Hourahine, B. Aradi, V. Blum, F. Bonafé, A. Buccheri, C. Camacho, C. Cevallos, M. Y. Deshayé, T. Dumitrică, A. Dominguez, S. Ehlert, M. Elstner, T. van der Heide, J. Hermann, S. Irle, J. J. Kranz, C. Köhler, T. Kowalczyk, T. Kubař, I. S. Lee, V. Lutsker, R. J. Maurer, S. K. Min, I. Mitchell, C. Negre, T. A. Niehaus, A. M. N. Niklasson, A. J. Page, A. Pecchia, G. Penazzi, M. P. Persson, J. Řezáč, C. G. Sánchez, M. Sternberg, M. Stöhr, F. Stuckenberg, A. Tkatchenko, V. W.-z. Yu and T. Frauenheim, *The Journal of Chemical Physics*, 2020, **152**, 124101.
- 5 M. Gaus, A. Goetz and M. Elstner, *Journal of Chemical Theory and Computation*, 2013, **9**, 338–354.
- 6 M. Gaus, X. Lu, M. Elstner and Q. Cui, *Journal of Chemical Theory and Computation*, 2014, **10**, 1518–1537.
- 7 P. Giannozzi, S. Baroni, N. Bonini, M. Calandra, R. Car, C. Cavazzoni, D. Ceresoli, G. L. Chiarotti, M. Cococcioni, I. Dabo, A. Dal Corso, S. de Gironcoli, S. Fabris, G. Fratesi, R. Gebauer, U. Gerstmann, C. Gougoussis, A. Kokalj, M. Lazzeri, L. Martin-Samos, N. Marzari, F. Mauri, R. Mazzarello, S. Paolini, A. Pasquarello, L. Paulatto, C. Sbraccia, S. Scandolo, G. Sclauzero, A. P. Seitsonen, A. Smogunov, P. Umari and R. M. Wentzcovitch, *Journal of Physics: Condensed Matter*, 2009, **21**, 395502.
- 8 J. Perdew, K. Burke and M. Ernzerhof, *Physical Review Letters*, 1996, **77**, 3865–3868.
- 9 S. Grimme, *Journal of Computational Chemistry*, 2006, **27**, 1787–1799.
- 10 A. Dal Corso, *Computational Materials Science*, 2014, **95**, 337–350.
- 11 G. Kresse and D. Joubert, *Phys. Rev. B*, 1999, **59**, 1758–1775.
- 12 G. J. Martyna and M. E. Tuckerman, *The Journal of Chemical Physics*, 1999, **110**, 2810–2821.
- 13 Marelli, E. and Casati, N. and Gozzo, F. and Macchi, P. and Simoncic, P. and Sironi, A., *CrystEngComm*, 2011, **13**, 6845.
- 14 Podsiadlo, M. and Olejniczak, A. and Katrusiak, A., *The Journal of Physical Chemistry C*, 2013, **117**, 4759.
- 15 Fabbiani, F.P.A. and Allan, D.R. and David, W.I.F. and Moggach, S.A. and Parsons, S. and Pulham, C.R., *CrystEngComm*, 2004, **6**, 504.

- 16 Rheingold, A.L., *CSD Communication*, 2016.
- 17 Adam, M.S. and Gutmann, M.J. and Leech, C.K. and Middlemiss, D.S. and Parkin, A. and Thomas, L.H. and Wilson, C.C., *New Journal of Chemistry*, 2010, **34**, 85.
- 18 Breton, G.W. and Martin, K.L., *Journal of Organic Chemistry*, 2002, **67**, 6699.
- 19 Talberg, H.J., *Acta Chemica Scandinavica [1989-1999]*, 1977, **31**, 485.
- 20 Castello-Mico, A. and Julia Nafe, and Higashida, K. and Karaghiosoff, K. and Gingras, M. and Knochel, P., *Organic Letters*, 2017, **19**, 360.
- 21 Ohkita, M. and Suzuki, T. and Nakatani, K. and Tsuji, T., *Chemistry Letters*, 2001, 988.
- 22 K.Mitsudo, T.Murakami, T.Shibasaki, T.Inada, H.Mandai, H.Ota, Seiji Suga, *Synlett*, 2016, **27**, 2327.
- 23 Chien-Yang Chiu, and Bumjung Kim, and Gorodetsky, A.A. and Sattler, W. and Sujun Wei, and Sattler, A. and Steigerwald, M. and Nuckolls, C., *Chemical Science*, 2011, **2**, 1480.
- 24 Mereiter, K. and Rosenau, T., *CSD Communication*, 2004.
- 25 Berridge, R. and Serebryakov, I.M. and Skabara, P.J. and Orti, E. and Viruela, R. and Pou-Amerigo, R. and Coles, S.J. and Hursthouse, M.B., *Journal of Materials Chemistry*, 2004, **14**, 2822.
- 26 Britton, D., *Acta Crystallographica Section E: Structure Reports Online [2001-2014]*, 2002, **58**, o637.
- 27 Maris, T., *CSD Communication*, 2016.
- 28 Panfilova, L.V. and Antipin, M.Yu. and Churkin, Yu.D. and Struchkov, Yu.T., *Khimiya Geterotsiklicheskikh Soedinenii*, 1979, 1201.
- 29 Lincke, G. and Finzel, H.-U., *Crystal Research and Technology*, 1996, **31**, 441.
- 30 Fang-Ming Miao, and Jin-Ling Wang, and Xiu-Shen Miao, ., *Acta Crystallographica, Section C: Crystal Structure Communications [1983-2014]*, 1995, **51**, 712.
- 31 Rabaca, S. and Oliveira, S. and Cerdeira, A.C. and Simao, D. and Santos, I.C. and Almeida, M., *Tetrahedron Letters*, 2014, **55**, 6992.
- 32 Morak, B. and Pluta, K. and Suwinska, K. and Grymel, M. and Besnard, C. and Schiltz, M. and Kloc, C. and Siegrist, T., *Heterocycles*, 2005, **65**, 2619.
- 33 Entwistle, R.F. and Iball, J. and Motherwell, W.D.S. and Thompson, B.P., *Acta Crystallographica, Section B: Struct. Crystallogr. Cryst. Chem. [1968-1982]*, 1969, **25**, 770.
- 34 Derissen, J.L. and Timmermans, C. and Schoone, J.C., *Crystal Structure Communications*, 1979, **8**, 533.
- 35 Newkome, G.R. and Joo, Y.J. and Theriot, K.J. and Fronczek, F.R., *Journal of the American Chemical Society*, 1986, **108**, 6074.
- 36 Aitipamula, S. and Pui Shan Chow, and Tan, R.B.H., *CrystEngComm*, 2010, **12**, 3691.
- 37 Hariprasad, V.M. and Nechipadappu, S.K. and Trivedi, D.R., *Crystal Growth and Design*, 2016, **16**, 4473.
- 38 Khatioda, R. and Bora, P. and Sarma, B., *Crystal Growth and Design*, 2018, **18**, 4637.
- 39 Aitipamula, S. and Wong, A.B.H. and Pui Shan Chow, and Tan, R.B.H., *CrystEngComm*, 2012, **14**, 8515.
- 40 Aitipamula, S. and Pui Shan Chow, and Tan, R.B.H., *CrystEngComm*, 2009, **11**, 1823.
- 41 Aitipamula, S. and Pui Shan Chow, and Tan, R.B.H., *Crystal Growth and Design*, 2010, **10**, 2229.
- 42 Aitipamula, S. and Pui Shan Chow, and Tan, R.B.H., *CrystEngComm*, 2009, **11**, 889.
- 43 Khatioda, R. and Saikia, B. and Das, P.J. and Sarma, B., *CrystEngComm*, 2017, **19**, 6992.
- 44 Kozak, A. and Marek, P.H. and Pindelska, E., *Journal of Pharmaceutical Sciences*, 2018, **108**, 1476.
- 45 Sarmah, K.K. and Boro, K. and Arhangelskis, M. and Thakuria, R., *CrystEngComm*, 2017, **19**, 826.
- 46 F. Musil, M. Veit, A. Goscinski, G. Fraux, M. J. Willatt, M. Stricker, T. Junge and M. Ceriotti, *The Journal of Chemical Physics*, 2021, **154**, 114109.
- 47 M. J. Willatt, F. Musil and M. Ceriotti, *Phys. Chem. Chem. Phys.*, 2018, **20**, 29661–29668.
- 48 *RDKit: Open-source cheminformatics.*, <https://www.rdkit.org>.
- 49 N. M. O'Boyle, M. Banck, C. A. James, C. Morley, T. Vandermeersch and G. R. Hutchison, *Journal of Cheminformatics*, 2011, **3**, 33.
- 50 *SMARTS: A Language for Describing Molecular Patterns*, 1997, daylight.com/dayhtml/doc/theory/theory.smarts.html.

- 51 F. Pedregosa, G. Varoquaux, A. Gramfort, V. Michel, B. Thirion, O. Grisel, M. Blondel, P. Prettenhofer, R. Weiss, V. Dubourg, J. Vanderplas, A. Passos, D. Cournapeau, M. Brucher, M. Perrot and E. Duchesnay, *Journal of Machine Learning Research*, 2011, **12**, 2825–2830.
- 52 Petricek, V. and Cisarova, I. and Hummel, L. and Kroupa, J. and Brezina, B., *Acta Crystallographica, Section B: Structural Science [1983-2012]*, 1990, **46**, 830.

- 68 Kumar, D. and Imler, G.H. and Parrish, D.A. and Shreeve, J.M., *Chemistry-A European Journal*, 2017, **23**, 7876.
- 69 Sheremetev, A.B. and Yudin, I.L. and Palysaeva, N.V. and Suponitsky, K.Yu., *Journal of Heterocyclic Chemistry*, 2012, **49**, 394.
- 70 Dianeze, M.J. and Lopez-Castro, A. and Marquez, R., *Acta Crystallographica, Section C: Crystal Structure Communications [1983-2014]*, 1985, **41**, 981.
- 71 A. Bauzá, T. J. Mooibroek and A. Frontera, *Chem. Comm.*, 2015, **51**, 1491–1493.
- 72 Khatioda, R. and Bora, P. and Sarma, B., *Crystal Growth and Design*, 2018, **18**, 4637.
- 73 Sarmah, K.K. and Boro, K. and Arhangelskis, M. and Thakuria, R., *CrystEngComm*, 2017, **19**, 826.
- 74 Khatioda, R. and Saikia, B. and Das, P.J. and Sarma, B., *CrystEngComm*, 2017, **19**, 6992.
- 75 Aitipamula, S. and Pui Shan Chow, and Tan, R.B.H., *CrystEngComm*, 2009, **11**, 1823.
- 76 Aitipamula, S. and Wong, A.B.H. and Pui Shan Chow, and Tan, R.B.H., *CrystEngComm*, 2012, **14**, 8515.
- 77 Hariprasad, V.M. and Nechipadappu, S.K. and Trivedi, D.R., *Crystal Growth and Design*, 2016, **16**, 4473.
- 78 Aitipamula, S. and Pui Shan Chow, and Tan, R.B.H., *Crystal Growth and Design*, 2010, **10**, 2229.
- 79 Kozak, A. and Marek, P.H. and Pindelska, E., *Journal of Pharmaceutical Sciences*, 2018, **108**, 1476.
- 80 Aitipamula, S. and Pui Shan Chow, and Tan, R.B.H., *CrystEngComm*, 2010, **12**, 3691.
- 81 Aitipamula, S. and Pui Shan Chow, and Tan, R.B.H., *CrystEngComm*, 2009, **11**, 889.
- 82 Pagola, S. and Stephens, P.W., *Acta Crystallographica, Section C: Crystal Structure Communications [1983-2014]*, 2009, **65**, o583.
- 83 Katsube, Y. and Sasada, Y. and Kakudo, M., *Bulletin of the Chemical Society of Japan*, 1966, **39**, 2576.
- 84 Reddy, L.S. and Babu, N.J. and Nangia, A., *Chemical Communications*, 2006, 1369.
- 85 Wei Xu, and Zheng Yang, and Xin-Hua Li, and Bo-Nian Liu, and De-Cai Wang, ., *Acta Crystallographica Section E: Structure Reports Online [2001-2014]*, 2009, **65**, o764.
- 86 Kostyanovsky, R.G. and Kostyanovsky, V.R. and Kadorkina, G.K. and Lyssenko, K.A., *Mendeleev Communications*, 2003, 111.
- 87 Larsen, I.K., *Acta Chemica Scandinavica [1989-1999]*, 1968, **22**, 843.
- 88 Kumasaki, M. and Kinbara, K. and Wada, Y. and Arai, M. and Tamura, M., *Acta Crystallographica Section E: Structure Reports Online [2001-2014]*, 2001, **57**, o6.
- 89 Fabbiani, F.P.A. and Allan, D.R. and David, W.I.F. and Davidson, A.J. and Lennie, A.R. and Parsons, S. and Pulham, C.R. and Warren, J.E., *Crystal Growth and Design*, 2007, **7**, 1115.
- 90 Fischer, N. and Klapotke, T.M. and Rappengluck, S. and Stierstorfer, J., *ChemPlusChem*, 2012, **77**, 877.
- 91 Kalman, A. and Simon, K. and Schwartz, J. and Horvath, G.,